Experimental results for structural design of Wire-and-Arc Additive Manufactured stainless steel members

(Article begins on next page)

20 April 2024

Vittoria Laghi, Michele Palermo, Giada Gasparini, Valentina Alena Girelli, Tomaso Trombetti

Experimental results for structural design of Wire-and-Arc Additive Manufactured stainless steel members

Experimental results for structural design of Wire-and-Arc Additive Manufactured stainless steel members

Vittoria Laghi*, Michele Palermo Ph.D, Giada Gasparini Ph.D, Valentina Alena Girelli Ph.D,

Tomaso Trombetti Ph.D

*corresponding author: vittoria.laghi2@unibo.it

Department of Civil, Chemical, Environmental and Materials Engineering - University of Bologna,

Viale del Risorgimento, 2 – 40136 Bologna, Italy

Abstract

Additive Manufacturing has gained great importance in the recent development to produce metallic structural elements for civil engineering applications. While a lot of research effort has been focused on different technologies (such as Powder Bed Fusion), there is still quite limited knowledge concerning the structural response of Wire-and-Arc Additive Manufactured (WAAM) metallic elements, as very few experimental campaigns aimed at assessing their geometrical and mechanical properties have been carried out. The paper presents selected results of a wide experimental campaign focused on the assessment of the main geometrical and mechanical properties of Wire-and-Arc Additive Manufactured (WAAM) stainless steel material, carried out at the Topography and Structural Engineering Labs from University of Bologna. In detail, the focus of the present study is on the characterization of the surface irregularities by means of various measuring techniques and on the main mechanical properties of the material, in terms of tensile and compressive strengths, Young's modulus and post elastic behavior. Tests results have been interpreted through statistical tools in order to derive mean values and gather information about the variability of both geometrical and mechanical parameters.

Key words

1. Introduction

Along the centuries, the evolution in building construction has always been strictly linked to significant advancements in material science, technology, industrial processes and engineering. As the first Industrial Revolution marked the use of metals as structural members, the improvement in scientific knowledge and the introduction of concrete at the beginning of XX century paved the way for Reinforced Concrete (RC) constructions ([1] Addis 2007). Similarly, in the last 30 years the way structures are designed, planned and built has changed completely with the technological innovations offered by software for Computer-Aided Design (CAD), which replaced manual drawings, without however changing the resulting architectural shapes. Only in the early years of the 21st century, a new design approach to architecture resulting in novel forms started to emerge by the utilization of three-dimensional computer modelling and digital fabrication methods. More recently, with what has been called the *digital turn* ([2] Carpo 2013), innovative computerized tools for architecture, structural and civil engineering have gained influence, enabling the design and construction of buildings with complex, doubly-curved geometry, such as shell structures and other free-form designs ([3] Adriaenssens et al. 2014).

The growth of automation since the beginning of 21st century has prevailed in almost all production domains with the exception of the building construction sector, in which the use of automatic tools is still challenging and at its first applications. The main challenge is due to some peculiar aspects of the construction industry: (i) building and civil constructions are very large-scale products requiring customization of conventional automated fabrication technologies; (ii) conventional design approaches are not tailored for automation; (iii) significantly smaller ratio of production quantity/type of final products as compared with other industries; (iv) limitations in the materials that could be employed by an automated system ([4] Koshnevis 2004). Only in the last few years, the fast development in digital fabrication techniques is leading towards applications in Structural Engineering field as well, through Additive Manufacturing (AM)-based technologies, already commonly used in other sectors such as aerospace, automotive and biomedical engineering ([5] Attaran 2017, [6] Thomas et al. 1996, [7] Song et al. 2002, [8] Giannatsis et al. 2009).

The term Additive Manufacturing has been attempted to be standardized in ISO/ASTM 52900 [9], where such terminology has been adopted for all processes of making parts from 3D models and materials. Nowadays Additive Manufacturing (AM) refers to the technology (or additive process) of depositing successive thin layers of material upon each other, as opposed to the traditional subtractive manufacturing, producing a final three-dimensional object, realized either in plastic, resin, rubber, ceramic, glass, concrete and metal. Recent reviews of the metal Additive Manufacturing processes

2

([10] Wong and Hernandez 2012, [11] Levandowski and Seifi 2016, [12] Sames et al 2016, [13] Everton et al. 2016, [14] Buchanan and Gardner 2019) distinguish them into three major categories: (i) Powder Bed Fusion (PBF); (ii) Directed Energy Deposition (DED) and (iii) sheet lamination.

In recent years research effort has been intensively dedicated to the study of PBF material fabrication and its specifications concerning building orientation and mechanical characteristics ([15] Skiba et al. 2009, [16] Niendorf et al. 2013, [17] Guan et al. 2013, [18] Yap et al. 2015; [19] Song et al. 2015, [20] Buchanan et al. 2017). ASTM F2792-10 ([21]) provides also an outline of metallic single-step Additive Manufacturing methods for this category of AM process. The PBF process, although presenting small geometrical imperfections and mechanical characteristics in the order of traditional stainless steel material, is limited by the build envelope of the equipment, which is typically a 250-mm cube ([20] Buchanan et al. 2017).

On the other hand, DED processes, and in particular Wire-and-Arc Additive Manufacturing (WAAM) technology, lies upon a more flexible building set-up, which consists of a "printing head" at the top of a robotic arm, allowing for the realization of elements without theoretical dimensional constraints. For such reason, it appears more suitable for structural engineering applications, for which the outputs requested are of the order of several meters (typically 3 to 5 m long). However, in order to obtain pieces of large dimensions, higher printing velocities are required, resulting in larger geometrical imperfections with respect to the digital model. Therefore, much effort is needed for a proper assessment of both the geometrical and mechanical characterization of the outputs from Wire-and-Arc Additive Manufacturing (WAAM) process.

2. Wire-and-Arc Additive Manufacturing for structural applications

2.1 The MX3D manufacturing process

A basic AM system consists of a combination of a motion system, heat source and feedstock ([10] Wong and Hernandez 2012). In particular, the combination of an electric arc as heat source and wire as feedstock is referred to as Wire-and-Arc Additive Manufacturing (WAAM), which currently uses standard off-the-shelf welding equipment, such as welding power source, torches and wire feeding system, while motion is provided by either robotic systems or computer numerical-controlled gantries. WAAM's layer height is commonly in the range of 1 to 2 mm, resulting in an expected surface roughness of about 0.5 mm for single track deposits. As a result, this process is not considered net shape, as machining is required to finish the part, thus being better suited for low- to medium-complexity and medium- to large-scale elements, as those implemented in Structural Engineering ([22] Williams et al. 2016, [23] Uziel 2016, [24] Haden et al. 2017, [25] Ji et al. 2017).

1 Among the various metal Additive Manufacturing technologies, the present work focuses on the

2 Wire-and-Arc Additive Manufacturing (WAAM) process developed by the Dutch company MX3D

3 ([26] www.mx3d.com) and adopted to realize the first 3D-printed steel footbridge (Figure 1) which

4 will be placed in the city center of Amsterdam by 2020 ([27] Joosten 2015, [28] van Bolderen 2017).

5 Indeed, the authors are partner in the "Bridge project" held by MX3D to run experimental tests for

6 the characterization of small specimens taken from planar sheets and full-scaled tubes.

7 MX3D makes use of gas metal arc welding, a process characterized by a continuous wire electrode

8 which is drawn from a reel by an automatic wire feeder, through the contact tip in the welding torch.

9 The heat is transferred from the welding arc and the internal resistive power causes the wire to melt

10 ([29] Kim et al. 2003, [30] Yilmax and Ugla 2017).

11 The motion system used by MX3D consists of industrial multi-axis ABB robots which, theoretically,

12 are able to print from any angle. Two different printing strategies have been explored by MX3D: a

13 so-called *continuous printing*, meaning that the material is deposited in continuous, and a so-called

14 *dot-by-dot printing*, meaning that the material is deposited by successive points. The effects of these

15 strategies on the metallurgic characteristics have been analyzed in [28]. The process used to realize

16 the MX3D Bridge [26] is a *continuous* printing strategy, and the welding wire used for the structure

17 under study is 308LSi austenitic stainless steel.

18 The fundamental process parameters are (i) the current and its voltage, (ii) the wire diameter, (iii) the

19 wire-feed rate, (iv) the welding speed and (v) the vertical printed layer height. The combination of

20 such controlling parameters affects the printing quality (geometrical precision and surface roughness)

21 as well as the material mechanical properties. Specifications on the parameters adopted in the

22 realization of the MX3D Bridge [26] are the following: 1-mm wire diameter, 0.6 to 2 mm/min wire-

23 feed rate, 15 to 30 mm/sec welding speed, 1 to 3 mm vertical printed layer height and an average total

24 printing speed of 0.5 to 2 kg/hour.

25 For Structural Engineering applications, the need of high welding velocity for a rapid realization of

26 structural elements of such proportions plays a crucial role for the specific characteristics of the

27 printed parts, as it induces geometric inaccuracy of the outcomes, both in terms of surface roughness

28 and lack of straightness of the elements. For a given element to be printed, a digital model from which

29 the printing head reads the coordinates of the points defining step by step the position of the welded

30 layer is created with Rhinoceros software ([31] http://rhino3d.com/). However, due to intrinsic

31 inaccuracy of the printing process, each point of the digital model has a real counterpart whose

32 position is not exactly the one of the digital model, as it is affected by an error.

Figure 1: *MX3D footbridge realized with WAM process and presented at the Dutch Design Week 2018 in Eindhoven [26].*

2.2 Objectives of the work

The specifications of the innovative manufacturing process are crucial to derive the response in terms of structural performances of the printed elements. The large velocity of deposition used to realize the specimens has induced some geometric irregularities which should be properly taken into account both in the design and construction phases. Moreover, the heating process induces some non-negligible residual stresses and deformation of the crystalized structure of the stainless steel, which may lead to an orthotropic behavior and should be further analyzed as well. For instance, Figure 2 provides different views of typical tubular elements manufactured by MX3D using the same continuous printing strategy as the one adopted for the realization of the MX3D Bridge. The photos allow to visually appreciate the typical geometrical imperfections resulting from the manufacturing process: cross-section shape irregularity (Figure 2a), lack of straightness (Figure 2b) and surface roughness (Figure 2c). These geometrical imperfections together with the specific material mechanical behavior related to the printing parameters affect the structural response of the printed elements and have to be fully addressed in order to provide valuable information to be used in the structural design.

In the present work the attention is focused on the geometrical and mechanical characterization of samples (planar specimens and hollow tubes) manufactured by MX3D using the Wire-and-Arc Additive Manufacturing process that has been used, for the first time in a civil engineering context, for the MX3D Bridge [26].

5

(a)   (b)   (c)

Figure 2: Geometric issues of WAAM tubular elements: (a) irregular cross-section; (b) lack of straightness; (c) surface roughness.

3. Geometrical and mechanical parameters of WAAM elements

In the present Section, meaningful definitions and quantities adopted to describe the geometrical and mechanical properties of the specimens and corresponding digital models are introduced. All quantities describing the geometry of the digital model will be hereafter indicated with the suffix "*n*", standing for "*nominal*", while those corresponding to the real printed element will be indicated with the suffix "*real*".

Two different categories of specimens are studied: rectangular plates of constant thickness (Figure 3) from which "dog-bone" shaped specimens have been obtained, and both hollow short (also referred to as stub columns) and long circular tubes of equal cross-section and various lengths (Figure 4).

3.1 Geometrical parameters

Considering the uniform rectangular plate represented in Figure 3, the origin of coordinate system used to describe the geometry of the plate is assumed to be located at one edge. The *x* and *y* axes are taken parallel to the two main directions of the plate, while the *z*-axis is perpendicular to the *x*-*y* plane. The thickness of the plate is given by the amount of welded metal positioned by the printing head, whose nominal value in the digital model is constant all over the plate and equal to t_n. On the other hand, the value of thickness in the printed plate is in general non constant and varies both with *x* and *y*, so that $t_{real}=t_{real}(x,y)$. Given that the plates have been produced with a certain printing direction, the surface roughness might have a different influence on the mechanical behavior of specimens cut along the printing direction (*x*) with respect to those cut perpendicular to it (*y*).
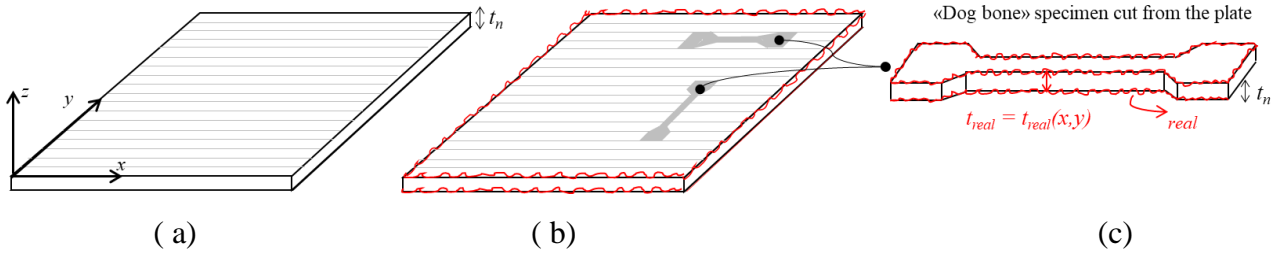
Figure 3: Digital model (a) and corresponding printed element (b) of a WAAM plate from which "dog-bone" specimens (c) are extracted.

Regarding the uniform hollow cylinder represented in Figure 4, a cylindrical coordinate system (r, z, θ) is adopted to describe the geometry of the tubular element, differentiating between the parameters used as inputs for the digital model (nominal values) and the corresponding values on the printed tube. The coordinate system has the origin in the centroid of the bottom cross-section. The z axis is coincident with the longitudinal axis of the digital model. For the digital model, the geometry of the tubular element is described by three scalar parameters only: the tube length (L_n), the outer diameter (D_n) and the thickness (s_n).
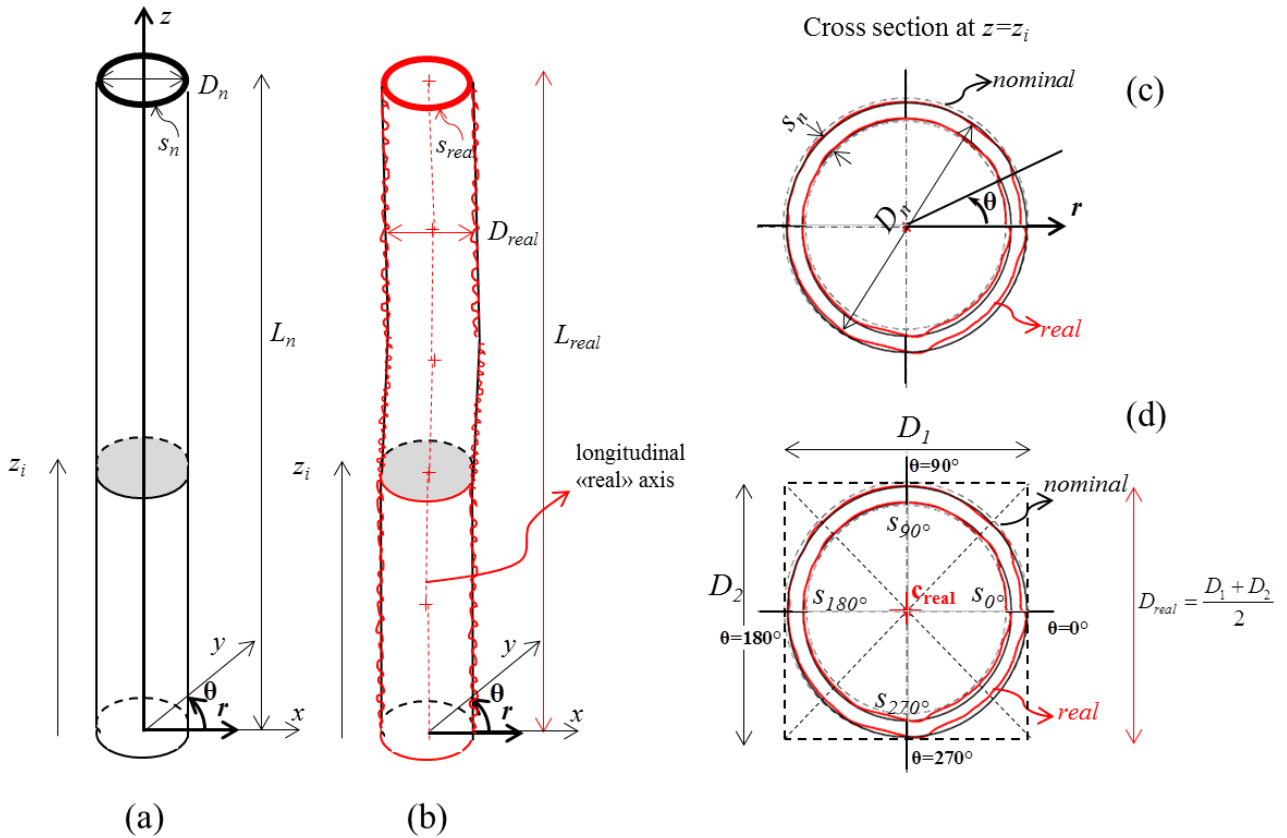

Figure 4: Digital model (a) and corresponding printed element (b) of a WAAM tube; polar coordinates along the section (c) and evaluation of outer diameter and thickness from printed outcome (d).

7

1   However, due to the intrinsic imperfections derived by the specific printing process, the outcome is

2   a tubular element with a non-perfectly hollow circular cross-section which varies over the height and

3   a non-straight longitudinal axis. In particular, both the real outer diameter D_{real} and the thickness s_{real}

4   vary with θ and z, e.g. $D_{real} = D_{real}(\theta, z)$ and $s_{real} = s_{real}(\theta, z)$. To reduce the variability of D_{real} to only

5   z variable, at each height z_i an equivalent outer diameter can be considered by constructing a

6   circumscribed rectangle with the four sides that are tangent to the outer surfaces at $\theta=0°$, $90°$, $180°$,

7    $270°$. The sides of the rectangle have lengths equal to D_1 and D_2, so that $D_{real} = \dfrac{D_1 + D_2}{2}$ is a function

8   of z only, e.g. $D_{real} = D_{real}(z)$. Similarly, at each height z_i the thickness can be computed as the average

9   over four measures taken at $\theta = 0°$, $90°$, $180°$ and $270°$, so that $s_{real} = \dfrac{s_{0°} + s_{90°} + s_{180°} + s_{270°}}{4}$. At each

10   height z_i the centroid of the tube (c_{real}) is obtained as the intersection of the two diagonals of the

11   circumscribed rectangle.

12

13   **3.2 Mechanical parameters**

14   The Wire-and-Arc Additive Manufacturing process (WAAM) is based on the deposition of fused

15   welding material from a wire feedstock. In particular, MX3D printing process adopts 308LSi stainless

16   steel as wire feedstock, therefore resulting in 3D-printed welded stainless steel elements.

17   Traditionally formed stainless steel is characterized, in general, by a highly non-linear behavior, thus

18   requiring specific parameters to identify the mechanical behavior.

19   In 1943 Ramberg and Osgood ([32] Ramberg and Osgood 1943) first introduced a simplified equation

20   to match the first part of the experimental stress-strain (σ-ε) curve, until a 0.2% proof stress ($\sigma_{0.2}$)

21   which conventionally is assumed as the yielding point of stainless steel:

22   $$\varepsilon = \frac{\sigma}{E_0} + 0.002\left(\frac{\sigma}{\sigma_{0.2}}\right)^n \tag{1}$$

23   where $n = \dfrac{\ln(20)}{\ln(\sigma_{0.2}/\sigma_{0.01})}$ (evaluated according to [33]) ensures that the Ramberg-Osgood equation

24   matches exactly the test values between 0.01% proof stress ($\sigma_{0.01}$) and 0.2% proof stress ($\sigma_{0.2}$), while

25   E_0 is the initial Young's modulus that can be evaluated according to Eurocode 3-14 [34]. The second

26   part of the stress-strain curve for stainless steel elements is usually evaluated according to Rasmussen

27   equation [33].

28

29

1 Traditionally manufactured 308LSi stainless steel grade attains mechanical properties in between

2 grade 304LSi and 316LSi, whose nominal values are given by various standards (see Table 1).

3 *Table 1:Summary of mechanical properties of grades 304LSi and 316LSi stainless steel for different standard provisions*

4 *[34, 35, 36].*

Grade		AS / NZS	SEI / ASCE	EC3 - 14
Austenitic 304 (EN 1.4301)	E_0 [GPa]	195	193.1	200
	$\sigma_{0.2}$ [MPa]	195 - 205	248.2 - 275.8	190 - 230
	σ_u [MPa]	520	551.6 - 620.6	500 - 540
Austenitic 316 (EN 1.4401)	E_0 [GPa]	195	193.1	200
	$\sigma_{0.2}$ [MPa]	195 - 205	248.2 - 275.8	200 - 240
	σ_u [MPa]	485	586.1 – 620.6	500 - 530

5

6 Since the manufacturing process may potentially induce an orthotropic behavior depending on the

7 orientation towards printing direction and the presence of surface roughness resulting from the

8 printing layers, the mechanical response will be investigated with reference to (1) samples with

9 artificially smoothed or as-manufactured surface, and (2) actions oriented along the printing direction

10 (also referred to as parallel direction) or perpendicular to it. Figure 5 shows a qualitative

11 representation of the different stress-strain response for three types of specimens subjected to tensile

12 action (F indicates the applied axial force). The following suffixes are used to indicate the mechanical

13 properties related to each type of samples: "s" standing for smoothed, "r" standing for rough, "\\"

14 standing for parallel, "_|_" standing for perpendicular.
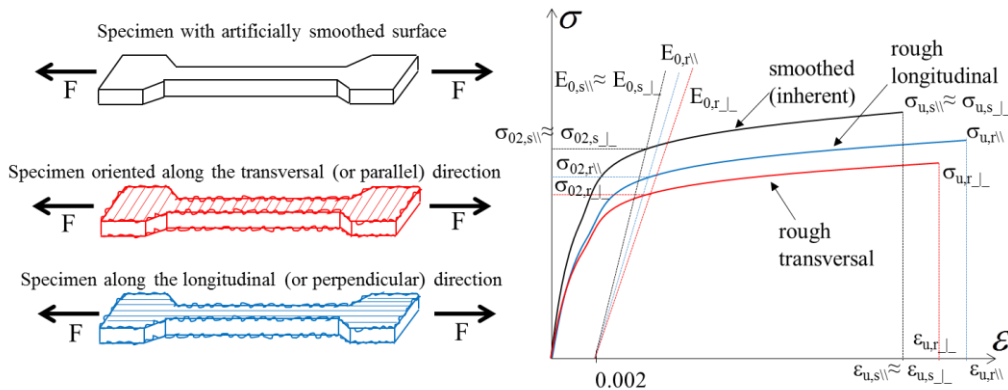
15

16 *Figure 5: Non-linear stress-strain curves of specimens with artificially smoothed surface and with rough surface oriented along the*

17 *printing (e.g. parallel) direction and along the orthogonal direction.*

For the purpose of the present work, the following mechanical parameters will be investigated from the experimental results: 0.2% proof stress ($\sigma_{0.2}$), ultimate stress (σ_u), Young's modulus (E_0), ultimate strain (ε_u).

4. Design considerations for WAAM elements

As introduced in the previous sections, structural elements manufactured with current WAAM processes are characterized by peculiar geometrical irregularities and specific material mechanical properties that have to be properly taken into account in both analysis and design process. Generally speaking, different approaches could be envisaged ranging from those based on advanced analysis and simulations able to model the real geometrical irregularities as well as material non-linearity, to simplified ones mainly developed for professional designers and compatible with current conventional analysis and design formats.

Theoretically speaking, the use of advanced simulation tools would allow to model the geometrical imperfections of each single manufactured piece and to consider the actual orthotropic non-linear stress-strain material behavior such that all the potential modes of failure could be explicitly included in the model. Such complex and detailed Finite Element models are also known as "digital twins" and would allow to even simulate loading tests, construction sequences, fatigue-related issues and other complex non-linear phenomena. These advanced analysis models may also be used along with structural monitoring systems for real-time control of the structural response. Pioneering research in this direction is currently under development by a research team led by Alan Turing Institute and MX3D in collaboration with Imperial College of London and Autodesk [37].

The full development of a reliable digital twin requires detailed knowledge of the peculiar geometrical imperfections requiring use of random field approaches and uncertainties quantification techniques ([38] Bae et al. 2004), as well as ad-hoc material models able to account for the specific features of WAAM. In order to properly manage such advanced simulation tools, structural engineers need to become more computationally literate and acquire high level computational skills ([14] Buchanan and Gardner 2019).

As an alternative to the advanced modelling of above, a simplified approach is here proposed. The idea lies upon decoupling the two main sources of variabilities: geometrical data and mechanical material properties.

As far as the geometrical characterization of each structural member is concerned, two types of results are derived: (1) general information on thickness and cross-sectional area then used for the

10

interpretation of the mechanical tests; (2) detailed information on surface roughness, lack of straightness, out-of-roundness, which could be used either for first engineering evaluations (within the scope of the present work) or for future works based on advanced modelling approaches.

As far as the mechanical material properties are concerned, the mechanical tests (developed with reference to the two main directions, i.e. parallel and perpendicular to the printing layer) are interpreted assuming that the cross-sectional area is constant along the member length so that the axial stresses can be computed according to simple beam theory:

$$\sigma_{eff} = \frac{F}{A_{eff}} \tag{2}$$

Where:

- A_{eff} is an effective cross-sectional area of the structural member to be determined on the basis of the result type (1) of above.

- F is the tensile axial force (e.g. the force applied during a tensile test). Clearly, the stress σ_{eff} can be interpreted as an effective stress which differs from the true material stress conventionally referred to as σ.

This result leads to condense all uncertainties (geometrical and mechanical) in the mechanical parameters only (see Section 6 for details). The simplified approach allows to treat the cross-sectional area as a deterministic value, while all the uncertainties are globally collected in the effective axial stress. In this way, the conventional format commonly adopted for the analysis and design of traditionally manufactured steel members, which considers the geometrical parameters as deterministic values and the material strength parameters as random variables, is maintained. Thus, the experimental mechanical parameters become dependent on both the specific geometrical and mechanical features related to the manufacturing process and not only on the material itself.

Clearly, the effective stresses σ_{eff} depend on A_{eff} and specific attention should be devoted to its choice. Different criteria can be adopted to chose A_{eff}, based on scientific, technical and practical considerations related to significance, accuracy and reliability of the chosen value. Some possibilities are (i) use of nominal values, (ii) use of a set of punctual values based on mechanical measurements, (iii) use of average values as obtained from volumetric measurements.

The use of nominal values as given by the manufacturer does not require any measurement, but, on the other hand, the absence of measurements may lead to lack of significance and poor reliability especially for non-standardized processes (like WAAM).

11

The use of few manual measurements (such as caliper measurements) is straightforward since such measurements can be easily executed even at the production site, but this type of measurements could be easily biased (see Sections 6.2 and 6.3).

The use of average values as obtained from volumetric measurements (used in the following proposed work to obtain A_{eff}, see details in Sections 6.2 ands 6.3) has the advantage of providing an integral value based on equal weight criterion. It can also be adopted for a fast quality control during the production phase.

5. The experimental campaign: methodological approach and work program

The work presents the first results of a wide experimental campaign carried out starting from January 2017 (and still on-going) at the Topography and Structural Engineering Labs from University of Bologna. The aim is to assess the geometrical and mechanical properties of WAAM real-scaled specimens realized by MX3D using the process specifications mentioned in Section 2.

5.1 The methodological approach: phases, measurements and mechanical tests

The phases of the experimental campaign have been defined in order to address the two most relevant issues from a structural design point of view, namely the intrinsic geometrical irregularities and the specific mechanical properties of WAAM elements.

The first phase is devoted to characterize the geometrical imperfections due to the adopted printing process, i.e. cross-section irregularities, surface roughness and lack of straightness. Since the evaluation of imperfections due to the manufacturing process may differ depending on the specific geometry to be printed, the specimens considered are both "dog-bone" shaped elements cut from rectangular plates and hollow circular tubes (stub columns and long tubes). Different types of measurements have been compared including: (i) punctual manual measurements with digital caliper with specific attention on the thickness for the "dog-bone" specimens and both thickness and outer diameter for the tubular specimens; (ii) volume-based measurements (from the Archimedes' principle) to obtain effective values of thickness for both types of specimens; (iii) 3D scan for a detailed evaluation of cross-section irregularities, surface roughness and lack of straightness of a single tubular element.

The second phase of the experimental campaign is devoted to the mechanical characterization of the printed outcomes, making use of fundamental information gathered from the previous phase. For this purpose tensile tests have been carried out on the "dog-bone" specimens cut from plates, compressive tests have been carried out on stub column specimens, and buckling tests have been performed on tubular elements. Photos of the tested specimens are shown in Figure 6.

Figure 6: Specimens produced by MX3D: (a) rectangular plate; (b) "dog-bone" shaped coupons; (c) stub columns. (d) hollow circular tubes.

5.2 The work program

The entire experimental work program is summarized in Table 2, providing an overview of the geometrical measurements and mechanical tests conducted on each sample. More in detail, the columns of Table 2 give the following information:

- Type: CS indicates "dog-bone" shaped specimens with smoothed surface; CR indicates "dog-bone" shaped specimens with rough surface; ST indicates short tubular specimens with rough surface (stub columns); LT indicates long tubular specimens with rough surface.
- Nominal dimensions: thickness for "dog-bone" specimens type; diameter, thickness and length for tubes type.
- Geometrical characterization: "Hand" indicates measurements with meter stick and caliper, "Volume" indicates volume-based measurements using the Archimedes' principle, "3D-scan" indicates measurements obtained through 3D scanner.
- Mechanical characterization: "Tensile" refers to tensile tests on "dog-bone" specimens, "Compression" refers to compression tests on stub columns, "Buckling" refers to the buckling tests on long tubes.

- Series (number of specimens): the series identifies a group of identical specimens. They are distinguished using Roman numbers. Within each series, the single specimens are distinguished with Arabic numbers.

- Identification code ID: the ID uniquely identifies each single specimen. The code is composed of the following symbols and numbers: T/C/B indicates the type of experimental tests (T stands for Tensile, C for Compression, B for Buckling); the Roman numeral refers to the Series (from I to VI), the Arabic number identifies the specific specimen of that Series. "x" and "y" apply to "dog-bone" specimens only and indicate their orientation ("x" refers to the specimens cut along longitudinal direction, i.e. along the printing layer, "y" refers to those cut along the transversal direction, i.e. perpendicular to it).

- Presented results: reports the type of information and results provided for each series in the paper. "G" indicates that results of the geometrical characterization are reported for that specific series. "M" indicates that the results of the mechanical characterization are reported for that specific series. "N" indicates that no results are reported for that specific series.

Table 2: Summary of specimens characteristics and tests.

Type	Nominal dimensions	Geometrical characterization	Mechanical characterization	Series (number of specimens)	Specimen ID	Presented Results
CS	t_n=4 mm	Hand	Tensile	I (2)**	TI-1-y and TI-2-x	G+M
CR	t_n=4 mm	Hand	Tensile	II (4)**	From TII-1-x to TII-4-x	G+M
CR	t_n=4 mm	Hand	Tensile	II (4) **	From TII-1-y to TII-4-y	G+M
ST	D_n= 55 mm, s_n=5 mm, L_n=150 mm	Hand Volume	Compression	III (9)	From CIII-1 to CIII-9	G+M
LT	D_n= 55 mm, s_n=5 mm, L_n=850 mm	Hand Volume 3D-Scan *	Buckling	IV (3)	From-BIV-1 to BIV-3	G*
LT	D_n= 55 mm, s_n=5 mm, L_n=1050 mm	Hand Volume	Buckling	IV (3)	From-BIV-4 to BIV-6	N
LT	D_n= 55 mm, s_n=5 mm, L_n=1200 mm	Hand Volume	Buckling	IV (3)	From-BIV-7 to BIV-9	N

14

CS	t_n=4 mm	Hand Volume	Tensile	V (10) **	From TV-1-x to TV-10-x	N
CS	t_n=4 mm	Hand Volume	Tensile	V (10) **	From TV-1-y to TV-10-y	N
CR	t_n=4 mm	Hand Volume	Tensile	VI (20) **	From TVI-1-x to TVI-20-x	G
CR	t_n=4 mm	Hand Volume	Tensile	VI (20) **	From TVI-1-y to TVI-20-y	G

* only specimen B-IV-3

** "dog-bone" specimens of Series I, II, V, VI belong to the same batch (for a total of 10 plates).

More in detail, the geometrical characterization (first phase) encompassed the following steps:

    a. Manual measurements on the first two Series (I and II) of "dog-bone" specimens cut from the rectangular plates;

    b. Manual measurements and volume-based measurements on stub column specimens (Series III) and on the further series of "dog-bone" specimens (Series V and VI);

    c. 3D scan of one tubular element (Series IV).

The analysis of part of the data obtained from the geometrical measurements is presented in Section 6.

More in detail, the mechanical characterization (second phase) encompassed the following steps:

- Tensile tests on 2 "smoothed" (e.g. two specimens whose surfaces have been artificially polished) "dog-bone" specimens (Series I) and on 8 "rough" (e.g. with as-manufactured external surfaces) "dog-bone" specimens (Series II) to derive the first average mechanical properties of WAAM metal material and first indications of possible anisotropy related to the printing direction;

- Compression tests on 9 stub column coupons (Series III);

- Buckling tests on 9 tubular elements (Series IV) with different values of global slenderness;

- Tensile tests on 20 "smoothed" (Series V) and 40 "rough" "dog-bone" specimens (Series VI) using Digital Imaging Correlation (DIC) for a more reliable assessment of the mechanical properties and variability including the anisotropy due to the printing direction.

As far as the mechanical characterization is concerned, for the sake of conciseness, only selected results will be presented in this paper: (i) the results from the tensile tests on Series I and II are presented and discussed in Section 7; (ii) the results from the compression tests on Series III are presented and discussed in Section 8.

Detailed interpretation and discussion of buckling tests (Series IV) and of the further series of tensile tests (Series V and VI) will be presented in further separate works. Indeed, the aim of the present work is to provide first basic information related to geometrical properties and irregularities resulting from the manufacturing process (such as effective cross-sectional area, surface roughness, lack of straightness, out-of-roundness) and key mechanical properties (Young's modulus, 0.2% proof stress and ultimate stress, both under tension and compression). This first information could then be useful to develop guidelines and recommendations for structural design purposes.

6. Geometrical characterization

As introduced in Section 4, the geometrical characterization provided two types of results:

1. General information on thickness and cross-sectional areas based on manual and volume measurement (Sections 6.2 and 6.3), here used to obtain the values of effective stresses from the mechanical tests.
2. Detailed information on surface roughness, lack-of-straightness and out-of-roundness based on 3D scan (Section 6.4).

As far as results type 1 is concerned, one of the main purpose is the evaluation of the discrepancies between the *nominal* (associated to the digital model), the *real* (as manufactured) and the *effective* values (used to compute the effective stresses) of cross-sectional area. Figure 7 provides a qualitative comparison between nominal, real and effective cross-sectional area for a tubular element manufactured through WAAM.

Hereafter in this work the values of the effective cross-sectional areas are those derived from volume measurements. For each specimen, the effective cross-sectional area can be expressed in terms of the nominal value by means of the correction factor φ ($A_{eff} = \varphi \cdot A_n$). In principle, φ could be treated as a random variable whose main descriptors (mean and coefficient of variation) can be determined from the results of geometrical measurements.
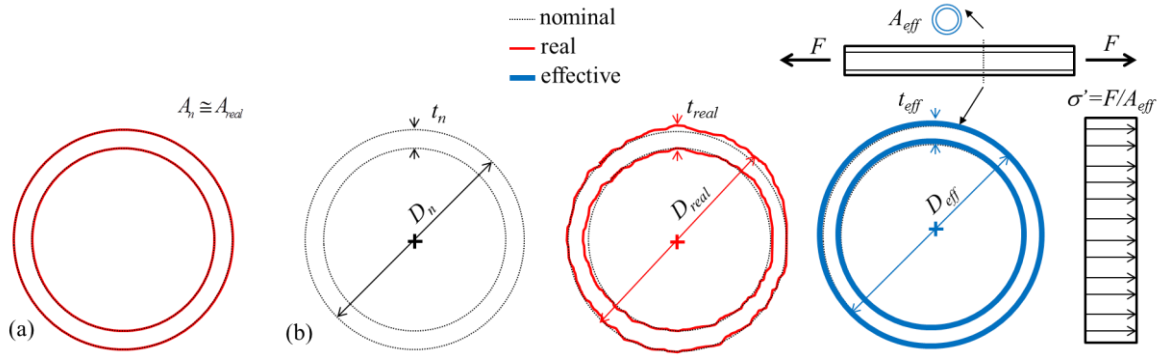
Figure 7: Tubular element: (a)manufactured with conventional techniques, (b) manufactured through WAAM (the difference between nominal, real and effective cross section is highligthed).

6.1. Measurements set-up

In order to assess the main geometrical parameters of Wire-and-Arc Additive Manufactured elements, the following measuring systems have been used:

    i.   Digital caliper (with a nominal precision of 0.02 mm) for manual measures. Measurements include: (i) thickness of "dog-bone" shaped specimens cut from rectangular plates (t_c, where suffix "c" refers to caliper measures) at various locations, (ii) outer diameter of hollow circular coupons (D_c, where suffix "c" refers to caliper measures) by taking the average dimension of the circumscribed rectangle of the cross-section, as described in Section 3.1, (iii) thickness of hollow circular coupons (s_c, where suffix "c" refers to caliper measures) at different heights (Figure 8a);

   ii.   Analogic hydraulic scale to take volume measurements from which the average thickness of both "dog-bone" shaped specimens ($t_{av,v}$, where suffix "v" refers to volume measures) and hollow circular coupons ($s_{av,v}$, where suffix "v" refers to volume measures) is derived (Figure 8b);

  iii.   3D scanning acquisition system for the evaluation of the cross-section irregularities, surface roughness and lack-of-straightness of one tubular element (Figure 8c).
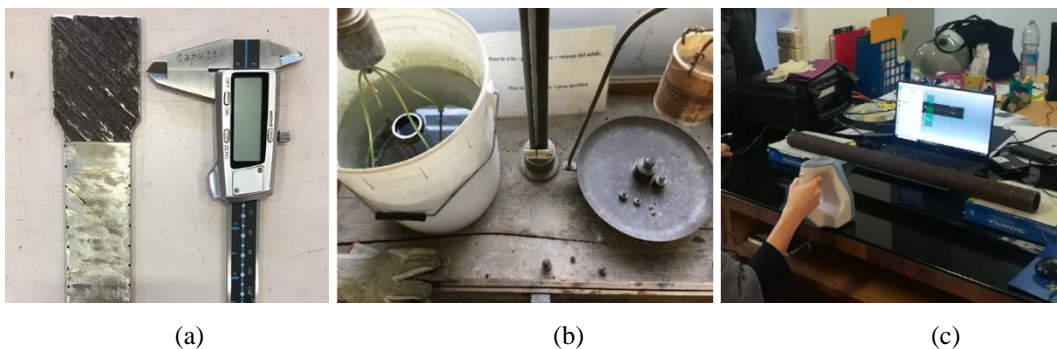
(a)   (b)   (c)

17

6.2. Thickness and cross-section of "dog-bone" specimens

In order to characterize thickness (t_{real}) and cross-sectional area (A_{real}) of "dog-bone" shaped specimens, two types of measures have been performed:

- Digital caliper measures of the main dimensions of the specimens and evaluation of thickness (t_c) at 3 different sections of each specimen (see Figure 9) to identify the average thickness ($t_{av,c}$). These measurements (see Table A1 in Appendix A) have been performed on all specimens of Series I, II (10 in total) and VI (40 in total).

- Volume measures from the Archimedes' principle, taking the weight on air (m_{air}) from a digital scale and the weight inside water (m_{H20}) from an analogic hydraulic scale. Based on the two measures taken on the weight, the specimens' volume has been derived from the calculated values of material density γ_v (see Table A2 in Appendix A) and density of water (at 25°C) γ_{H20} with the following formulation: $V = (m_{air} - m_{H_2 0}) / \gamma_{H_2 0}$. Then, the real average thickness ($t_{av,v}$) of the specimen has been computed dividing the volume by the specimen surface area (computed from the measures of the external geometry taken with digital caliper). These measurements have been performed on Series VI specimens (40 in total).

For each specimen of Series VI, the ratio χ between the average thickness obtained from caliper measurements ($t_{av,c}$) and that from volume measurements ($t_{av,v}$) has been computed.

Tables A1 and A2 in Appendix A report all the measured values for Series I, II and VI. For Series I, the mean value of thickness (over 2 specimens) as obtained from caliper measurements results equal to 2.92 mm, while for Series II the mean (over 8 specimens) results equal to 4.38 mm with a coefficient of variation of 0.04. For Series VI, the mean value of thickness (over 40 specimens) as obtained from caliper measurements results equal to 4.52 mm with a coefficient of variation equal to 0.07. The mean value of thickness as obtained from volume measurements for specimens of Series VI results equal to 3.92 mm with a coefficient of variation equal to 0.10.

The measurements indicate that, on average, the thickness as obtained from caliper measurements ($t_{av,c}$) is slightly larger (+13%) than the nominal value (t_n=4 mm). On the contrary, the average value of thickness as obtained from volume measurements ($t_{av,v}$) is slightly less (-2%) than the nominal value (t_n). For Series VI, the average value of coefficient χ results equal to χ_{av}=1.16. The discrepancy between caliper measures and volume measures results from the nature of the surface roughness, having very sharp peaks and troughs as qualitatively shown in Figure 9. Indeed, the caliper

18

measures are representative of thickness values taken around the peaks, given the practical difficulty of obtaining measurements close to the troughs. As a consequence, the resulting average values ($t_{av,c}$) tend to be larger than those obtained through volume measurements, which can be considered as some sort of integral values over the entire surface, thus accounting for both contributions of the peaks and troughs. In addition, the difference between the average thickness from volume measurements and the nominal thickness can be interpreted as a systematic error due to limited precision of the manufacturing process. In light of this, the values of thickness derived from volume measurements can be considered as effective values, since they correspond to those of an equivalent specimen with constant (effective) thickness having equal volume. The ratio between the average values of thickness from volume measurements $t_{av,v}$ and the nominal thickness t_n represents the mean value of the correction factor φ which results equal to φ_{av} =0.78, with a coefficient of variation of 0.10.

Regarding Series II specimens, for which no volume measurement was taken, the value of the effective cross-sectional area (then used for the calculation of the stresses, see Section 7) has been obtained dividing the average value obtained from caliper measurements ($A_{av,c}$) by the factor χ_{av} =1.16 (calibrated based on measurements on specimens from Series VI). The assumption is justified by the common nature of the surface roughness of Series II and Series VI, as all plates were manufactured with the same printing strategy and deposition method.
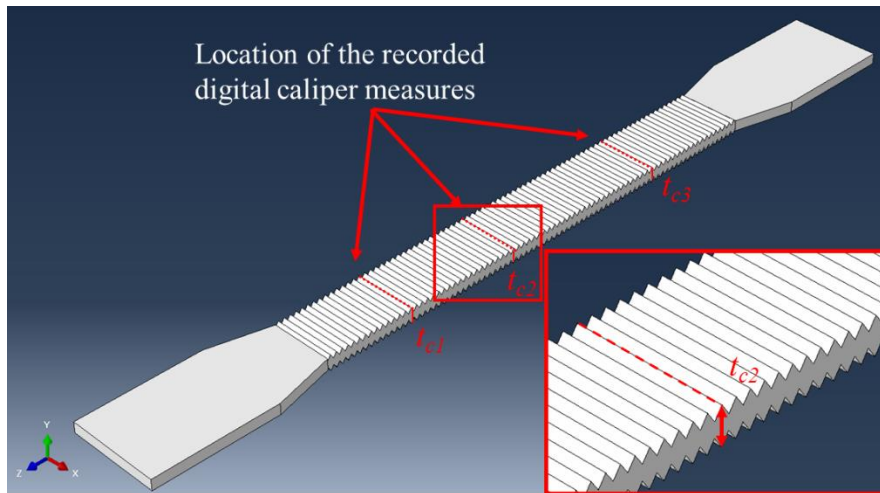
Figure 9: Location of the digital caliper measurements and detail of one measurement.

6.3. Thickness, cross-section and outer diameter of stub columns coupons

In order to characterize the geometry (cross-sectional area and thickness) of 9 stub columns coupons (Series III), two types of measures have been performed, following the same approach described in the previous Section:

1   •   Digital caliper measures of outer diameters (D_c) and thickness (s_c) taken at 3 different heights

2   z_i (e.g. 40 mm, 80 mm and 120 mm) to identify the average real outer diameter ($D_{av,c}$) and

3   cross-sectional area ($A_{av,c}$).

4   •   Volume measures from the Archimedes' principle, taking the weight on air (m_{air}) from a

5   digital scale and the weight inside water (m_{H20}) from an analogic hydraulic scale. Based on

6   the same procedure as the one described in Section 6.3, from the measures of the specimens

7   volume and length (L_c), the average cross-sectional area $A_{av,v}$ has been obtained. Then, based

8   on the values of the outer diameter taken from digital caliper measures (D_c) and assuming

9   circular hollow cross-section, the average thickness ($s_{av,v}$) of the specimen has been derived.

10 For each specimen, the ratio χ between the average thickness as obtained from caliper measurements

11 ($s_{av,c}$) and from volume measurements ($s_{av,v}$) has been computed.

12 Table A3 in Appendix A provides the results from the measures listed for each of the 9 specimens of

13 Series III. The mean value (over the 9 specimens) of the average diameter $D_{av,c}$ as obtained from

14 caliper measurements results equal to 53.97 mm. The coefficient of variation results less than 0.01,

15 indicating a quite reduced variability with respect to the other geometrical quantities here evaluated.

16 The maximum discrepancy between the measured average diameter $D_{av,c}$ and the nominal outer

17 diameter ($D_n = 55$ mm) is equal to 1.40 mm corresponding to a relative error of 2.50%. It should be

18 noted that the tolerances in terms of outside dimensions for cold-formed welded circular hollow

19 sections as given by various standard provisions ([39] EN 10219-2:2006, [40] EN 10162:2003, [41]

20 EN 10051:2010) are ± 1 % with a minimum of ± 0.3 mm and a maximum of ±1.0 mm.

21 The mean value of thickness (over the 9 specimens) as obtained from caliper measurements $s_{av,c}$

22 results equal to 5.25 mm, with a coefficient of variation of 0.04. The mean value of thickness (over

23 the 9 specimens) as obtained from volume measurements $s_{av,v}$ results equal to 3.81 mm, with a

24 coefficient of variation of 0.03. For each single specimen, the thickness from volume measurement

25 ($s_{av,v}$) is obtained from the measured volume and the average outer diameter $D_{av,c}$. Then, the average

26 outer diameter ($D_{av,c}$) is used together with the thickness from volume measurement to compute the

27 volume-based area ($A_{av,v}$), assumed as effective area. Overall, the thickness values as obtained from

28 digital caliper measures ($s_{av,c}$) are, on average, slightly (+5%) larger than the nominal value

29 (s_n=5mm). On the contrary, the thickness values (e.g. the effective thickness) as obtained from

30 volume measurements ($s_{av,v}$) are, on average, smaller (-23.70%) than the nominal value. Moreover,

31 the mean value of the correction factor of the cross-sectional area (φ) results equal to φ_{av}=0.85. The

32 coefficient of variation is equal to 0.02. The larger discrepancy between the nominal and effective

33 thickness for the stub columns coupons (-23.70%) can be interpreted as a sort of systematic error

rather than a consequence of random variability, since the coefficient of variation of volume measurements for stub columns coupons results smaller than the one of "dog-bone" specimens (COV=0.03 for stub columns coupons against COV=0.10 for "dog-bone" specimens of Series VI). The stress values computed from the compressive test results (described in Section 8) are based on the volume measurements ($A_{av,v}$), considered as effective.

6.4.   3D scan of one tube (BIV-3)

One of the WAAM tubular elements (e.g. specimen BIV-3) then tested for buckling has been first scanned by means of high resolution 3D scanning. The equipment consists of an optical non-contact measuring system based on the blue light, therefore on the principles of topographic triangulation. The projected fringe pattern of blue light on the object surface evidences distortions due to the specimen's surface shape. For the present work, two cameras have been adopted to capture the distortion and calculate the corresponding 3D coordinate measurements, acquiring full-field scans of a volumetric area and collecting millions of points per scan.

The structured-light projection Artec Spider scanner ([42] https://www.artec3d.com) adopted for the present work has an acquisition speed of 1 mln points/sec for metrology applications. The 3D resolution obtained is of 100 points/mm^2, with a 3D point accuracy of 0.05 mm for a medium field size of 90x70 mm and a working distance of 0.25 m.

The obtained 3D model of the tubular specimen consists of around 40 million of triangular elements, with a medium size of about 0.10 mm. Figure 10 shows a view of the entire mesh of the real tube (blue model), as compared with the digital model (grey model), as well as a zoom of a portion to better appreciate the surface roughness and two cross-sections referred to as sections A and B.
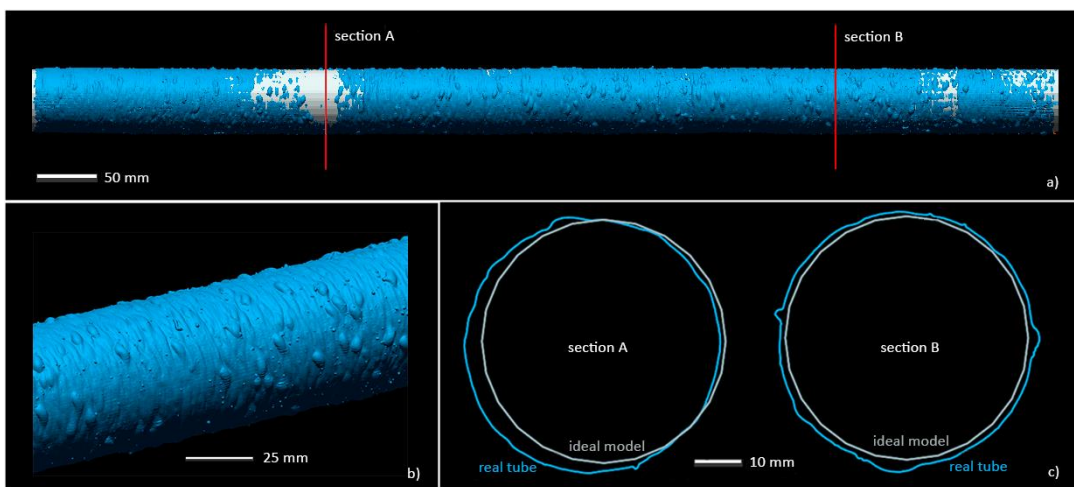
The data obtained from the 3D scan of one tubular specimen (e.g. BIV-3) have been processed to obtain a first characterization of the main external surface irregularities (such as variation of the outer diameter along the length and variation of the surface roughness both along the length and with respect to angle θ) and of the global geometrical imperfections (such as lack of straightness, out-of-roundness) relevant from a structural design perspective. For this aim, a number of 40 cross-sections spaced at 20 mm along the longitudinal axis extracted from the complete 3D model (Figure 11) has been analyzed. Clearly, for an accurate study of the surface features a more refined discretization would be required (providing data at cross-sections spacing of the order of 0.5 mm so that both peaks and troughs would be properly captured). Nevertheless, such detailed geometrical analysis is out of the scope of the present paper.

Each of the 40 cross-sections has been analyzed according to the schematization of Figure 4 with the purpose of obtaining the values of D_s (suffix "s" stands for the measures taken from 3D scanner acquisition) and the coordinates of the centroid $c_{real}=(c_{real,x}, c_{real,y})$. Note that at each cross-section the outer diameter D_s has been taken from the dimensions of the circumscribed rectangle, as described in Section 3.1. Since only the external surface has been scanned, the coordinates of the centroid have been computed as the center of the circumscribed rectangle, thus implicitly assuming a constant wall thickness for each cross section. Details of the measures taken at each cross-section are listed in Table A4 of Appendix A.
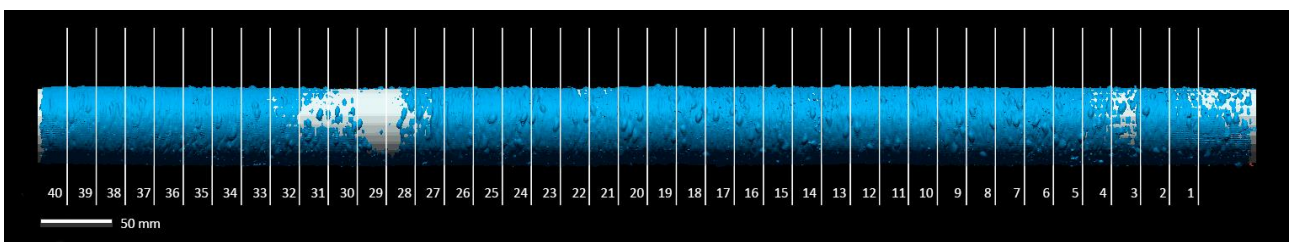
Figure 11: Model of real tubular element from 3D scanning acquisition.

6.4.1. Outer diameter

From the evaluation of the 40 cross-sections taken on the 3D scan, the resulting mean and standard deviation of D_s along the tubular element are equal to $\mu_{Ds}=53.48$ mm and $\sigma_{Ds}=0.39$ (corresponding to a COV=0.01). On average, the relative error in the real outer diameter with respect to the digital model, e.g. $(D_n-\mu_{Ds})/ D_n$, is equal to 2.76%. Figure 12 shows that the experimental CDF of the real

1   outer diameter can be well fitted by a Gaussian distribution (for the sake of comparison also the Log-

2   normal distribution which fits the data has been plotted in the graph).

3

4

5   (a)   (b)
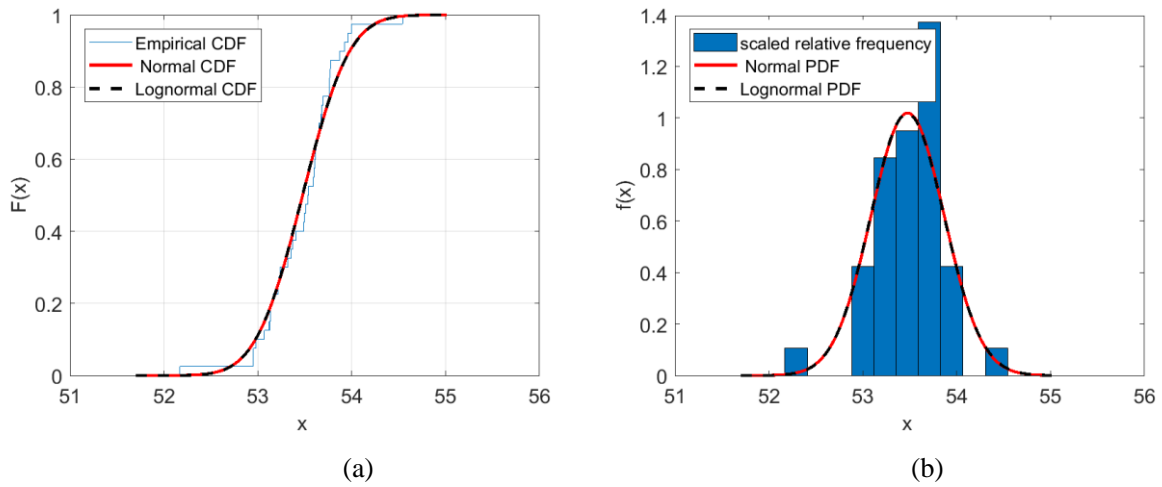
6   *Figure 12: Distribution of outer diameter values: (a) cumulative distribution functions (CDFs); (b) probability density functions*

7   *(PDFs).*

8

9   *6.4.2. Surface roughness*

10   The data of the 3D scan have also been used to analyze the surface roughness of the tubular element.

11   In particular, for each of the 40 selected cross-sections, 4 measures of the outer radius r have been

12   taken, each one at a different angle θ (e.g. *$\theta=0°$, $\theta=90°$, $\theta=180°$, $\theta=270°$*) as shown in Figure 4.

13   Figure 13 displays all the measured values of the outer radius along the longitudinal axis,

14   distinguishing each measurement angle with a different color. The thin continuous black line indicates

15   the constant value of the radius in the digital model, equal to $D_n / 2=27.5$ mm, while the thick dotted

16   black line corresponds to the average value of the outer radius at the 40 sections considered, equal to

17    $D_{av,s} / 2=26.74$ mm. The discrepancies between the real outcome of the printing process and the digital

18   model vary along the z-axis and with respect to the angle of rotation θ, thus indicating a non-uniform

19   roughness both along the length of the element and along the cross-section at each cutting plane.

20   However, it should be noted that the discrepancy between the average value obtained from 3D

21   scanning data ($D_{av,s} / 2$) and the digital model ($D_n / 2$) is of around 0.75 mm (corresponding to a
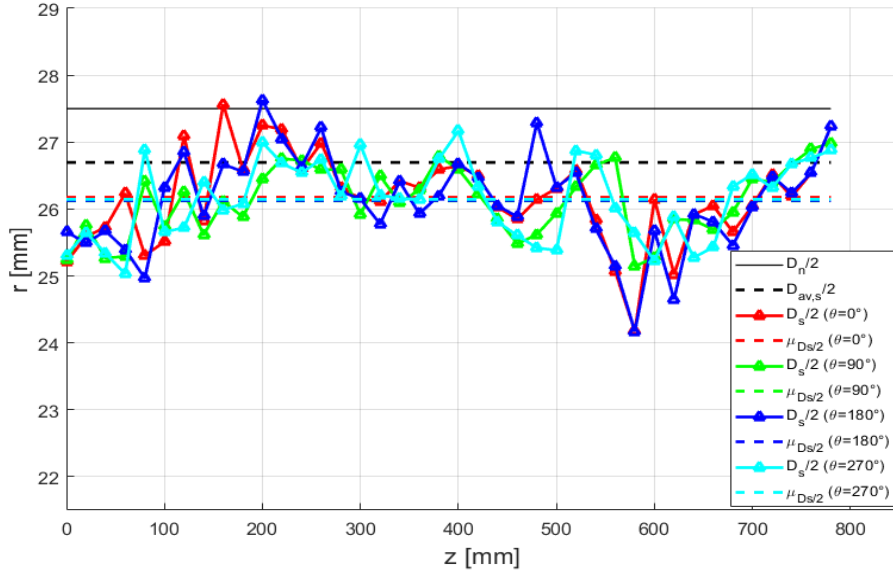
22   relative error of 2.70%).

23

Figure 13: Surface roughness along longitudinal axis over 4 points of the external surface: at $\theta=0°$, $\theta=90°$, $\theta=180°$, $\theta=270°$.

6.4.3. Lack of straightness

The data obtained from the 3D scanning are also used to evaluate the lack of straightness of the longitudinal axis (along z direction), considering the same 40 cross-sections of Figure 11. For each cross-section the lack of straightness is computed as the distance between the z-axis and the centroid of the circumscribed rectangle (c_{real}). The distance corresponds to the coordinates of the centroid ($c_{real,x}$, $c_{real,y}$ using Cartesian x-y coordinates or $c_{real,r}$ using cylindrical coordinates). Figure 14 displays the piece-wise line that connects the centroids of the 40 cross-sections (c_{real}), which can be defined as the "real longitudinal axis" of the printed tube (see Figure 4), while Table 3 provides numerical values of maximum, minimum and average discrepancies between the real longitudinal axis (thick blue line) and the z-axis (thin black line). The maximum (absolute value) of the lack of straightness is of L/300, while the average is of around L/1000.

It is important to note that steel beams/columns manufactured with conventional technologies (laminated profiles) generally have minimum geometrical imperfections in the order of L/1000 ([40] EN 10162:2003). In addition, for cold-formed welded tubular members, the tolerance in straightness is of L/500 according to EN 10219-2 [38]. It should be remarked that, in general, the lack of straightness depends upon two contributions: (1) global crookedness due to WAAM nature (layer-by-layer deposition); (2) possible local centroid deviation due to variation of wall thickness with θ (Figure 4c). Nonetheless, at first approximation, the contribution due to local centroid deviation could be considered negligible with respect to the global crookedness. Therefore, the values computed are based on the assumption of constant wall thickness for each cross-section since the centroid

24

coordinates have been determined as the center of the circumscribed rectangles. For a more precise
evaluation of the local variation in the thickness, a complete 3D scanning of the inner part of the tube
would be required as well.
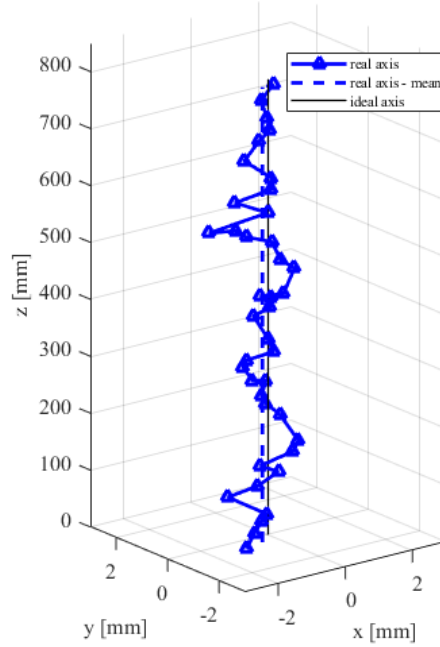
Figure 14: Study of straightness of longitudinal axis.

Table 3: Summary of study of longitudinal axis.

Longitudinal axis	$c_{real,x}$ [mm]	$c_{real,y}$ [mm]	$\lvert c_{real,r} \rvert$ [mm]	$c_{real,x}/L$ [%]	$c_{real,y}/L$ [%]	$\lvert c_{real,r} \rvert /L$ [%]
max	0.51	0.38	2.52	0.06	0.05	0.32
min	-2.39	-1.44	0.06	-0.30	-0.18	0.01
μ	**-0.46**	**-0.38**	**0.81**	**-0.06**	**-0.05**	**0.10**
COV	**1.23**	**1.22**	**0.61**	**1.23**	**1.22**	**0.61**

Figure 15 shows that the experimental CDF of the real longitudinal axis is quite asymmetric and
therefore can be well fitted by a Log-normal distribution (for the sake of comparison also the Gaussian
distribution fitting the experimental data is plotted in the graph). It can be noted that the Gaussian
distribution does not well fit the experimental data. This is due to a significant asymmetry and very
large coefficient of variation (around 0.60) of the experimental data.
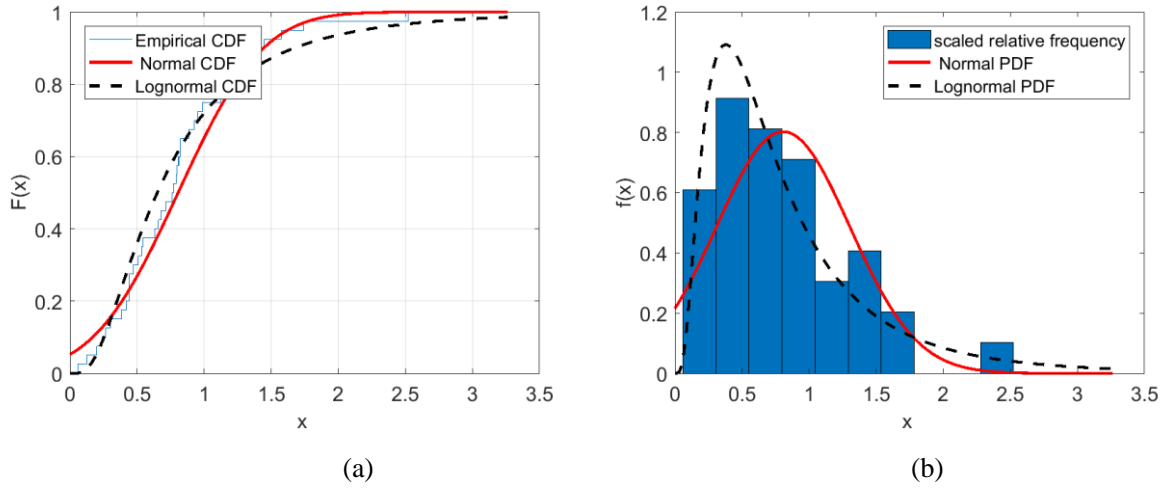
Figure 15: Distribution of longitudinal axis values: (a) cumulative distribution functions (CDFs); (b) probability density functions (PDFs).

6.4.4. Out-of-roundness

The out-of-roundness (O) values have been computed considering the 40 cross-sections of Figure 11. For each cross-section, out-of-roundness values are computed using D_1 and D_2 values (see Figure 4) according to the following equation: $O(\%) = \dfrac{|D_2 - D_1|}{D_n} \cdot 100$. The mean value of $O(\%)$ along the 40 cross-sections results equal to 1.31%, with a coefficient of variation of 0.70. The maximum value of $O(\%)$ results equal to 3.20%. Figures 16 shows the experimental CDF and the relative frequency histogram of the out-of-roundness ($O\%$). It can be noted that the data are quite uniformly distributed within the domain. For traditionally cold-formed welded circular hollow cross-sections the maximum out-of-roundness tolerance is equal to 2% according to EN 10219-2 [38]. ISO 19902 [43] provides maximum out-of-roundness tolerance of 3% for fixed steel offshore structures.
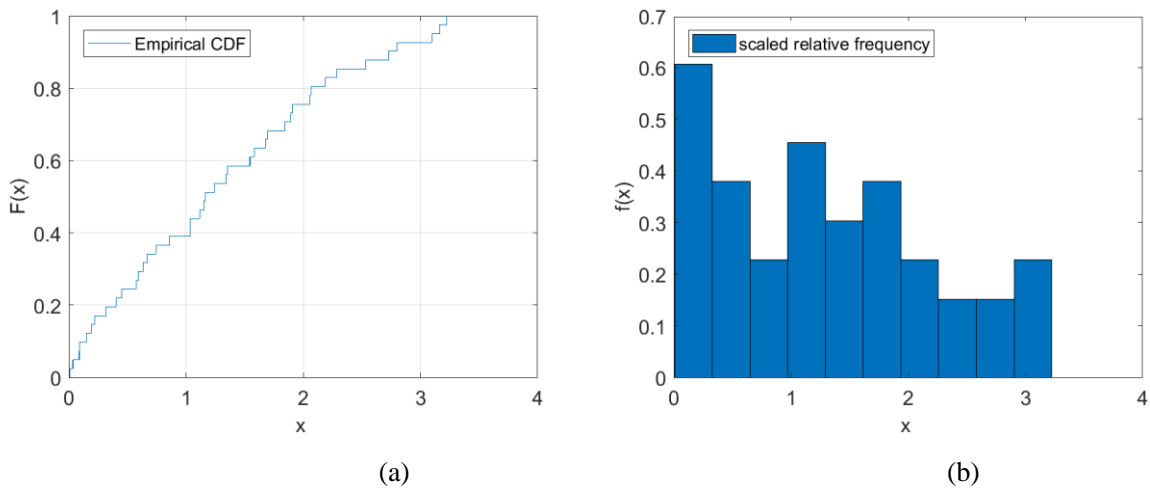
Figure 16: Distribution of out-of-roundness values: (a) cumulative distribution functions (CDFs); (b) relative frequency histogram.

26

7. Tensile coupon tests (series I and II)

The first experimental campaign aimed at assessing the mechanical behavior of the printed material under tensile loading has been carried out in 2017 over a number of 10 samples (Series I and II). The preliminary results of part of the experimental tests have been presented in a previous work done by the authors ([44] Laghi et al. 2018).

7.1. Specimens and set-up

The tensile test specimens are cut along the two main directions of the Additive Manufactured stainless steel plates, as described in Section 3.1 (see Figure 3), following the provisions in terms of shape and dimensions for tensile test samples described in ISO 6892-1:2016 ([45]). The longitudinal direction, referred to as x, has been taken parallel to the printed layers, while the transversal direction, referred to as y, perpendicular to that. The response from the different orientation of the specimens would give first useful information regarding the anisotropy and build orientation influence of WAAM manufacturing technique.

Among the 10 specimens tested, the specimens from Series I (TI-1-y and TI-2-x) have been previously artificially polished with milling cutter in order to reduce the surface roughness and thus have a first valuation of the mechanical properties on the material itself, reducing the influence of geometrical surface irregularities.

The tests have been performed using a Universal Machine of 600 kN nominal tensile capacity by applying the tensile load at a rate of 1 MPa / sec. The longitudinal elongation of each specimen is measured using a Linear Variable Differential Transformer (LVDT). Figure 17 shows the adopted testing set-up.
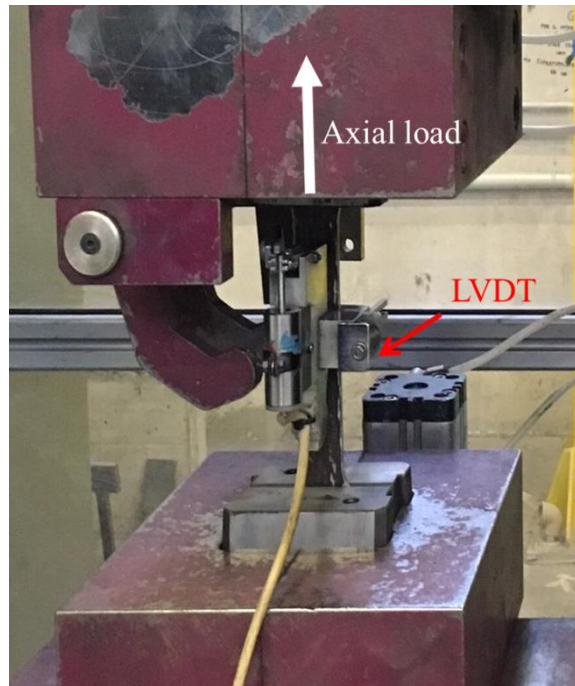
Figure 17: Experimental set-up of the tensile tests on "dog-bone" specimens.

7.2. Test results

The stress-strain diagrams as obtained from all tensile tests of Series I and II are shown in the graphs of Figure 18, separating the two "smoothed" specimens of Series I (Fig. 18 a and b), from the "rough" specimens of Series II, oriented along the longitudinal direction (x) (Fig. 18 c and d) and along the transversal direction (y) (Fig. 18 e and f). As explained in Section 6.2, for the specimens belonging to Series II, the stresses are obtained dividing the recorded values of loads by the effective cross-sectional area assumed to be equal to $A_{av,c}$ / χ_{av}. Values of strains are taken from the measures recorded by the LVDT. Table 4 collects the numerical values of the main mechanical parameters.

Overall, the stress-strain material behavior presents a fundamental difference with respect to conventional structural stainless steel material in terms of Young's modulus (E_0), whose values result to be between 108 to 152 GPa, with an average of 115 GPa. This corresponds to 60% of the usual Young's modulus of cold-formed stainless steel suggested by common standard provisions [34, 35, 36] (equal to 200 GPa, as shown in Table 1). The reduced Young's modulus values observed for WAAM material might be due to several factors: (i) the intrinsic residual stresses given by the temperature gradient between added layers of welded material; (ii) the different microstructure of Wire-and-Arc Additive Manufactured metal material, as highlighted by recent research works ([46, 47]). However, further investigation on these factors is needed in order to give proper explanation of such behavior. On the other hand, the values of the other significant response parameters (0.2% proof

28

1   stress $\sigma_{0.2}$ and ultimate stress σ_u) are closer to those of traditionally manufactured stainless steel (see

2   Table 1). In particular, the values of 0.2% proof stress $\sigma_{0.2}$ are larger (+50%) than those given by the

3   codes reported in Table 1, while the ultimate stresses σ_u are within the ranges.

4   As far as the behavior along the two directions is concerned, some discrepancies can be noted. First

5   of all, from the graphs providing the stress-strain responses at low strains (<1%, e.g. Fig. 18 b, d, f)

6   the response of the specimens cut along the transversal direction (*y*) appears smoother, as more

7   rounded stress-strain response can be appreciated already at low values of stresses. Moreover,

8   specimens cut along the transversal direction (*y*) result in lower mechanical properties when

9   compared to those cut along the longitudinal direction (*x*). In more details, the reductions are: 13%

10   for 0.2% proof stresses $\sigma_{0.2}$, 9% for ultimate stresses σ_u , 19% for Young's modulus E_0 and 32% for

11   ultimate strain ε_u.

12

13   (a)   (b)

15

16   (c)   (d)

29

(e)   (f)
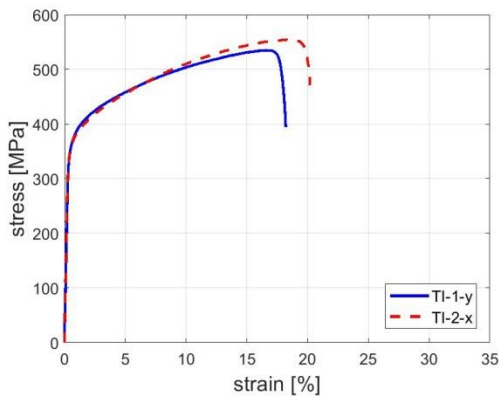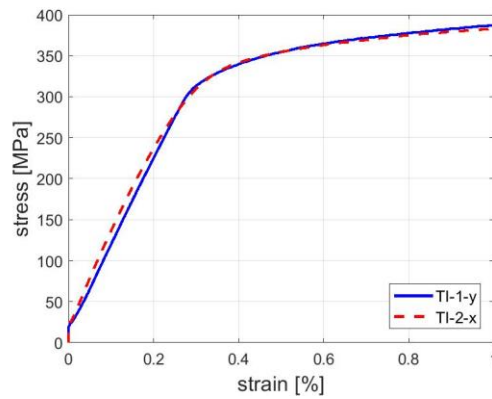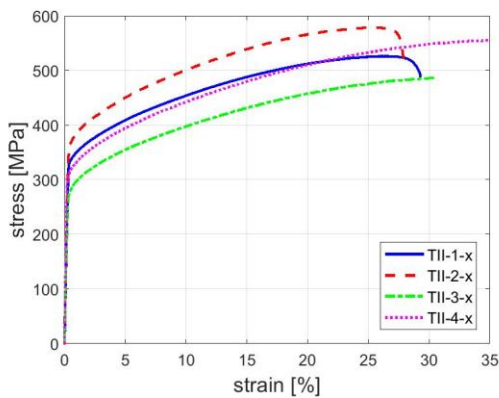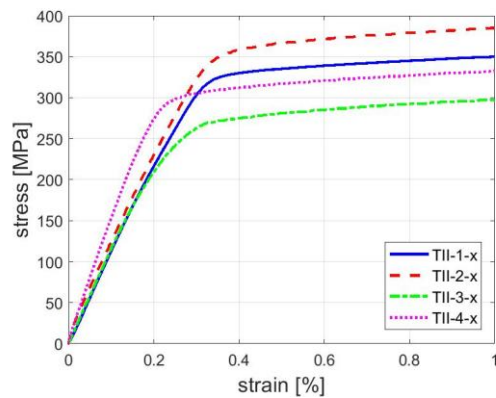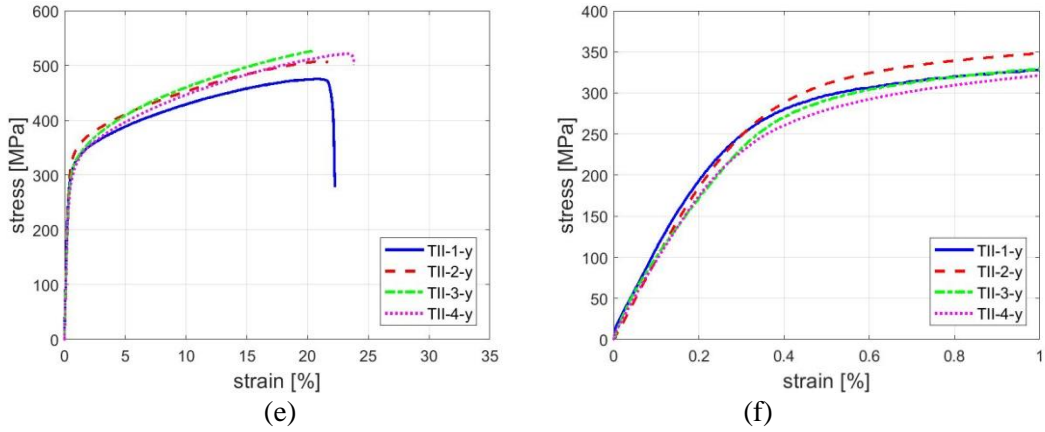
Figure 18: Stress-strain curve from tensile tests data. Series I: (a) full response; (b) zoom for strain < 1%. Series II:(c) full response (specimens oriented along x direction);(d) zoom for strain < 1% (specimens oriented along x direction); (e) full response (specimens oriented along y direction); (f) zoom for strain < 1% (specimens oriented along y direction)

Table 4: Results from tensile tests (Series I and II).

Specimen	$\sigma_{0.2}$ **[MPa]**	σ_u **[MPa]**	ε_u **[%]**	E_0 **[GPa]**
TI-1-y	355	535	18	108
TI-2-x	353	554	20	113
TII-1-x	364	558	29	119
TII-2-x	384	613	28	118
TII-3-x	302	517	33	121
TII-4-x	338	588	40	152
μ	**347**	**569**	**33**	**128**
COV	**0.08**	**0.06**	**0.13**	**0.10**
TII-1-y	315	505	22	106
TII-2-y	333	539	22	102
TII-3-y	267	485	20	101
TII-4-y	298	553	24	105
μ	**303**	**521**	**22**	**104**
COV	**0.07**	**0.05**	**0.06**	**0.02**

8. Stub column tests

The second part of the experimental campaign presented in Section 5.2 has been devoted to assess the behavior in compression of Wire-and-Arc Additive Manufactured stainless steel material, with a total number of 9 stub columns tested under monotonic compressive load (Series III).

30

8.1. Specimens and set-up

The stub columns have a nominal length L_n of 150 mm, a nominal outer diameter D_n of 55 mm and a nominal thickness s_n of 5 mm from the digital model. The tests are conducted with the same Metrocom testing machine used for the tensile tests (Figure 19). The monotonic compressive load is applied at a constant speed of 1 MPa / sec. The longitudinal elongation of the specimen is measured using two Linear Variable Differential Transformers (LVDTs) positioned at two sides.

Figure 19: Experimental set-up of the compression tests on stub column specimens.

The main aim of the tests is to investigate the behavior up to yielding in order to compare the values of Young's modulus and 0.2% proof stress with those obtained from the tensile tests. Indeed, due to the initial out-of-straightness, the specimens can be subjected to combined compression and bending mainly influencing the post-elastic behavior and local buckling mode of failure. Figure 20 evidences the deformed configurations at the end of the test for three different specimens. It can be noted that the local buckling modes of failure are quite different from each other. However, detailed interpretation of the failure modes is out of the scope of the present work.

(a)   (b)   (c)
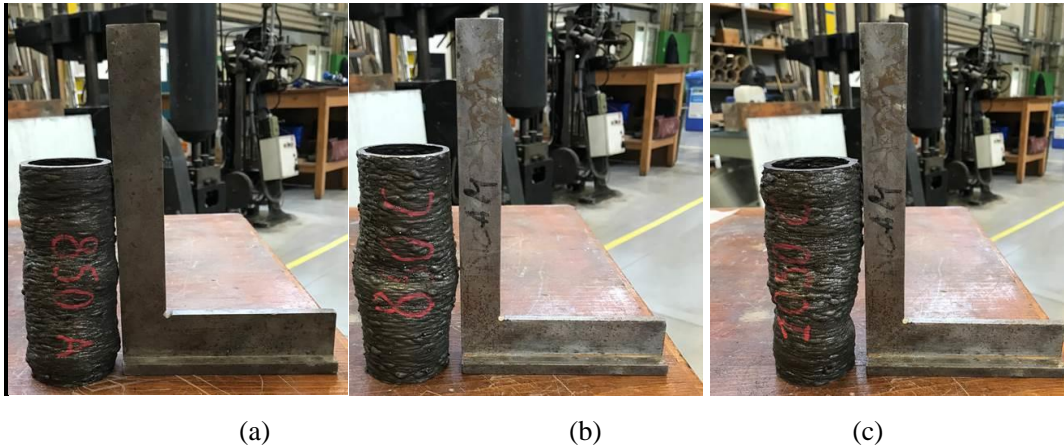
Figure 20: Deformed configuration of stub column coupons at the end of the test: (a) specimen CIII-1; (b) specimen CIII-3; (c) specimen CIII-6.

8.2. Test results

The stress-strain diagrams obtained from the tests of Series III are shown in graphs of Figure 21. The values of effective cross-sectional areas from volume measurements ($A_{av,v}$) as described in Section 6.3 are considered to compute the stresses from the recorded values of forces. Values of strains are computed as the average between the values recorded by the two LVDTs at the two sides of the specimen. It has been verified that, up to the first yielding, the deformation values recorded by the two LVDTs remained close enough to each other so that the average deformation can be considered as representative of the axial strain. Table 5 collects the numerical values of the main mechanical parameters.

As first evaluation it can be noted that the elastic behavior in compression is similar to the one observed from the tensile tests, with Young's modulus values (E_0) around 100 GPa, and 0.2% proof stress $\sigma_{0.2}$ values around 300 MPa. The ultimate stress and strain values (σ_u and ε_u) are affected by the specific kind of local buckling failure and therefore can be used as a reference only for similar specimens (e.g. hollow circular specimens with diameter/thickness ratio equal to 10). Moreover, the compressive specimens tend to have a rounded stress-strain response, as visible from Figure 21b, similar to the behavior of "dog-bone" shaped specimens cut along the transversal direction (Series II), as visible from Figure 18f.

It can be of interest to notice that the local buckling mode of failure was highly influenced by the presence of the geometrical imperfection and typically resulted in an asymmetric deformed configuration (see Figure 20). Nonetheless, specimen CIII-1 exhibited a more symmetric mode of failure resulting in an overall increase in the peak stress (equal to roughly 530 MPa and closer to the

32

1   values obtained from the tensile tests) without the typical final drop evidenced by the stress-strain

2   curves of most of the specimens.
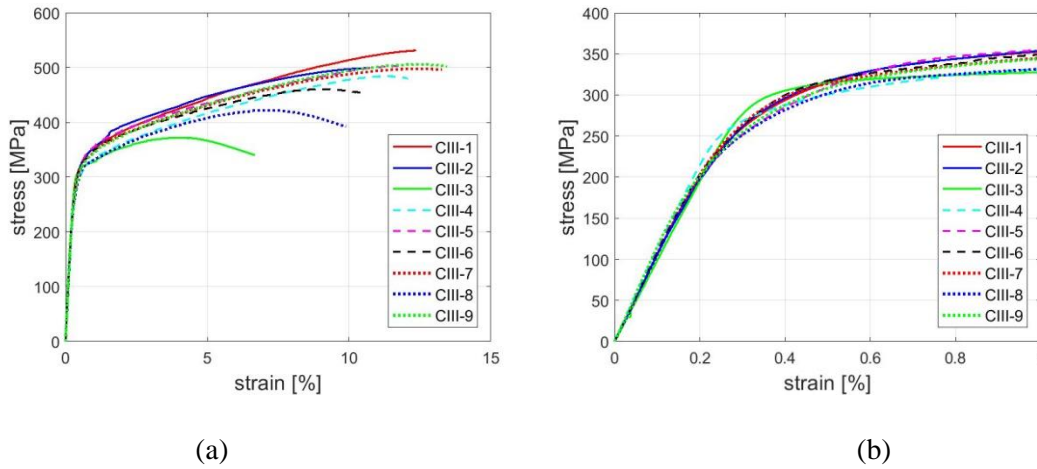
4   (a)   (b)

7   *Table 5: Results from compressive tests (Series III).*

Specimen	$\sigma_{0.2}$ [MPa]	σ_u [MPa]	ε_u [%]	E_0 [GPa]
CIII-1	317	531	12	106
CIII-2	318	499	11	95
CIII-3	317	372	7	98
CIII-4	293	484	12	102
CIII-5	303	502	12	106
CIII-6	317	461	11	103
CIII-7	308	498	13	104
CIII-8	294	422	10	104
CIII-9	299	506	13	115
μ	**307**	**475**	**11**	**104**
COV	**0.03**	**0.10**	**0.16**	**0.05**

9. Discussion of the mechanical tests results

10 Although the results presented in the previous sections are based on limited number of samples

11 (especially the ones related to smooth specimens of Series I), they provide first indications useful for

12 structural design purposes as well as to plan future experimental campaigns.

13 Tables 6 provides the values of key mechanical parameters obtained from of the experimental tests

14 with reference to smoothed and rough surfaces, tested along the parallel and perpendicular directions

15 with respect to the printing layer, both in tension and in compression.

33

The mechanical properties from tensile tests on artificially smoothed samples either in terms of Young's modulus, 0.2% proof stress $\sigma_{0.2}$ and ultimate stress σ_u seem to be practically coincident in both longitudinal and orthogonal directions (with relative differences off less than 5%). This indicates that the printing direction may not lead to an orthotropic behavior of the base material.

The mechanical properties from tensile tests on rough (as manufactured) samples indicates that Young's modulus, 0.2% proof stress $\sigma_{0.2}$ and ultimate stress σ_u along the transversal direction are smaller than the corresponding values along the parallel directions (relative differences of 10-20%). This indicates that the surface irregularities may lead to a geometrically-induced orthotropic behavior of the structural members.

The mechanical properties from compression tests on rough (as manufactured) samples, relative to the orthogonal direction only, indicate that both Young's modulus and 0.2% proof stress $\sigma_{0.2}$ are practically coincident to the corresponding ones from tensile tests. On the other hand, ultimate stress in compression σ_u shows a reduction of about 10% with respect to the one from tensile test, due to the specific buckling failure mode. This indicates that neither the geometrical irregularities nor the thermal effects (and their combination) associated with WAAM manufacturing process induces significant asymmetric tension-compression behavior (up to yielding) of the structural members.

Table 6: Summary of the experimental test results .

	Tensile					Compression (rough, _|_)
	Smoothed surface		Rough surface			
	\\	_|_	\\	_|_	Relative difference	
E_0 [MPa]	113	108	128	104	-19%	104
$\sigma_{0.2}$ [MPa]	353	355	347	303	-13%	307
σ_u [MPa]	554	535	569	521	-8%	475

Conclusions

In the paper, the results of a first experimental campaign aimed at characterizing the geometrical and mechanical properties of Wire-and-Arc Additive Manufactured (WAAM) stainless steel structural members are presented. The main goal of this first work is to draw some preliminary considerations useful for structural design and planning future exhaustive experiment campaigns.

Firstly, the attention has been paid on the geometrical characterization. Results obtained from manual measurements, volume-based measurements and 3D scanning acquisition system have been analyzed and compared. In details, the effort has been focused in (i) evaluating the discrepancies between the

nominal and the effective thickness of the specimens extracted from the planar plates which have been quantified, on average, in the order of +-0.5 mm (+-10% of the nominal value), (ii) evaluate the discrepancies between the nominal and the effective cross-section outer diameter of hollow tubes, quantified in the order of -2 mm (-25% of the nominal value) and (iii) evaluate the lack of straightness of hollow tubes which can be quantified, at first approximation, as an initial imperfection with maximum value of about 1/300 of the member length.

Secondly, the main mechanical parameters of WAAM stainless steel material have been investigated through tensile tests on artificially polished samples where all geometrical imperfections were removed. The most relevant outcome from a structural design point of view is the resulting low value of Young's modulus for WAAM elements, in the order of 110-130 GPa, highly reduced with respect to traditionally manufactured stainless steel material. Nonetheless, values of 0.2% proof stresses as well as ultimate stresses are in line with those of traditionally manufactured stainless steel material. Also, the obtained results indicate that the mechanical behavior of the basic material is not affected by the orientation of the specimen with respect to the printing direction.

Finally, the mechanical properties of as-manufactured structural specimens have been investigated through tensile and compression tests. In order to account for the geometric imperfections, a simplified approach has been introduced to interpret the experimental results based on the concept of effective cross-sectional area which could be useful also for design purposes. The obtained results indicate that the mechanical behavior of as-manufactured pieces is affected (through the geometrical imperfections) by the orientation of specimen with respect to the printing direction. Indeed, the specimens cut perpendicular to the direction of printing layer (e.g. transversal direction) have reduced strengths with respect to those cut along the printing direction (e.g. longitudinal direction). In details, 0.2% proof stress and ultimate stress along the transversal direction are respectively reduced of about 10% with respect to those along the longitudinal direction. Also Young's modulus in the transversal direction is reduced of about 20% with respect to the one along the longitudinal direction. Moreover, no evident asymmetric behavior in tension and compression has been observed up to yielding.

Overall, the tests indicate a marked orthotropic behavior of WAAM members with geometrical irregularities due to the manufacturing process. On the other hand, the WAAM material seems not exhibiting an orthotropic behavior.

35

Notation list

The following symbols are used in this paper:

$A_{av,c}$ = average cross-sectional area from caliper hand measurements;

$A_{av,v}$ = averge cross-sectional area from volume-based measurement;

A_{eff} = effective cross-sectional area;

A_{real} = effective cross-sectional area from printed specimen;

D_1 = first dimension of the circumscribed polygon;

D_2 = second dimension of the circumscribed polygon;

$D_{av,c}$ = average outer diameter from caliper hand measurements;

$D_{av,s}$ = average outer diameter from 3D scan measurements;

D_c = outer diameter from caliper hand measurement;

D_n = outer diameter from digital model;

D_{real} = real outer diameter from printed element;

D_s = outer diameter from 3D scan measurement;

E_0 = Young's modulus;

$E_{0,r\backslash\backslash}$ = Young's modulus values from rough specimens cut along the printing layer;

$E_{0,r\_\perp}$ = Young's modulus values from rough specimens cut perpendicular to the printing layer;

$E_{0,s\backslash\backslash}$ = Young's modulus values from artificially smoothed tensile specimens cut along the printing layer;

$E_{0,s\_\perp}$ = Young's modulus values from artificially smoothed tensile specimens cut perpendicular to the printing layer;

F = axial force applied to the specimen;

1     $L_{av,c}$ = average specimen length from caliper hand measurement;

2   L_c = specimen length from caliper hand measurement;

3   L_n = specimen length from digital model;

4   L_{real} = real specimen length from printed element;

5   O = out-of-roundness;

6   V = volume measure;

7   c_{real} = position of the cross-sectional centroid taken from 3D scan measurements;

8     $c_{real,r}$ = radial coordinate of the position of the cross-sectional centroid taken from 3D scan
9   measurements;

10    $c_{real,x}$ = x-coordinate of the position of the cross-sectional centroid taken from 3D scan measurements;

11    $c_{real,y}$ = y-coordinate of the position of the cross-sectional centroid taken from 3D scan measurements;

12   m_{air} = specimen mass measured in air;

13   m_{H2O} = specimen mass measured inside water;

14   n = Ramberg-Osgood parameter;

15   r = polar coordinate corresponding to the value of radius along the tubular specimen;

16    $s_{av,c}$ = average thickness of circular hollow specimens from caliper hand measurements;

17    $s_{av,v}$ = average thickness of circular hollow specimens from volume-based measurements;

18   s_c = thickness of circular hollow specimens from caliper hand measurement;

19   s_n = nominal thickness of circular hollow specimens from digital model;

20   s_{real} = effective thickness of circular hollow specimens from printed element;

21    $t_{av,c}$ = average thickness of "dog-bone" specimens from caliper hand measurements;

22    $t_{av,v}$ = average thickness of "dog-bone" specimens from volume-based measurements;

23   t_c = thickness of "dog-bone" specimens from caliper hand measurement;

24   t_n = nominal thickness of the plate from digital model;

1   t_{real} = real thickness of the plate from printed element;

2   ε = value of strain (for Ramberg-Osgood equation);

3   ε_u = ultimate strain (at rupture);

4   γ_{H2O} = average density of water;

5   γ_v = average density of specimen from volume measurement;

6   μ = mean value from distributions;

7   μ_{Ds} = mean value from distribution of outer diameter values taken from 3D scan at 40 cross sections;

8   σ = value of stress (for Ramberg-Osgood equation);

9   σ_{Ds} = standard deviation of distribution of outer diameter values taken from 3D scan at 40 cross

10   sections;

11   σ_{eff} = effective axial stress;

12     $\sigma_{0.01}$ = 0.01% proof stress;

13     $\sigma_{0.2}$ = 0.2% proof stress;

14     $\sigma_{0.2,r\backslash\backslash}$ = 0.2% proof stress values from rough specimens cut along the printing layer;

15     $\sigma_{0.2,r\_\perp}$ = 0.2% proof stress values cut from rough specimens cut perpendicular to the printing layer;

16     $\sigma_{0.2,s\backslash\backslash}$ = 0.2% proof stress values from artificially smoothed tensile specimens cut along the printing

17   layer;

18     $\sigma_{0.2,s\_\perp}$ = 0.2% proof stress values from artificially smoothed tensile specimens cut perpendicular to

19   the printing layer;

20   σ_u = ultimate stress;

21     $\sigma_{u,r\backslash\backslash}$ = ultimate stress values from rough specimens cut along the printing layer;

22     $\sigma_{u,r\_\perp}$ = ultimate stress values cut from rough specimens cut perpendicular to the printing layer;

23     $\sigma_{u,s\backslash\backslash}$ = ultimate stress values from artificially smoothed tensile specimens cut along the printing layer;

24     $\sigma_{u,s\_\perp}$ = ultimate stress values from artificially smoothed tensile specimens cut perpendicular to the

25   printing layer;

26   φ = correction factor for cross-sectional area ($t_{av,v}/t_n$);

27   φ_{av} = average value of correction factor for cross-sectional area;

χ = ratio between thickness measures taken from caliper and thickness taken from volume measures $(t_{av,c}/t_{av,v})$.

χ_{av} = average value of χ.

References

[1] W. Addis, "Building: 3000 Years of Design Engineering and Construction", Phaidon Press, London/New York, 2007.

[2] M. Carpo (ed.), "The Digital Turn in Architecture 1992-2012", John Wiley & Sons, Hoboken, 2013.

[3] S. Adriaenssens, P. Block, D. Veenendaal and C. Williams (eds.), "Shell Structures for Architecture: Form Finding and Optimization", Routledge, Abingdon, 2014.

[4] B. Khoshnevis, "Automated Construction by Contour Crafting – Related Robotics and Information Technologies", Automation in Construction, vol.13, no. 1, pp. 5-19, 2004.

[5] M. Attaran, "The Rise of 3-D Printing: The Advantages Of Additive Manufacturing Over Traditional Manufacturing", Business Horizons, vol. 60, no. 5, pp. 677-688, 2017.

[6] C.L. Thomas, T.M. Gaffney, S. Kaza, C.H. Lee, "Rapid prototyping of large scale aerospace structures". Proceedings of Aerospace Applications Conference IEEE. Aspen, CO, vol.4, pp.219–230, 1996.

[7] Y. Song, Y. Yan, R. Zhang, D. Xu, F. Wang, "Manufacturing of the die of an automobile deck part based on rapid prototyping and rapid tooling technology". Journal of Materials Processing Technology, vol.120, no.1-3, pp. 237–242, 2002.

[8] J. Giannatsis, V. Dedoussis, "Additive fabrication technologies applied to medicine and health care: a review". International Journal of Advanced Manufacturing Technology, vol.40, no.1-2, pp. 116–127, 2009.

[9] ASTM International, "ISO/ASTM 52900:2015: Standard terminology for additive manufacturing technologies – general principles - terminology". American Society for Testing and Materials, ASTM International, 2015.

[10] K.V. Wong and A. Hernandez, "A review of additive manufacturing." ISRN Mechanical Engineering, 2012.

[11] J.J. Lewandowski, M. Seifi, "Metal additive manufacturing: a review of mechanical properties." Annual Review of Materials Research, vol.46, pp. 151-186, 2016.

[12] W.J. Sames, F.A. List, S. Pannala, R.R. Dehoff, S.S. Babu, "The metallurgy and processing science of metal additive manufacturing." International Materials Reviews, vol. 61, no. 5, pp. 315-360, 2016.

[13] S.K. Everton, M. Hirsch, P. Stravroulakis, R.K. Leach, A.T. Clare, "Review of in-situ process monitoring and in-situ metrology for metal additive manufacturing." Materials & Design, vol. 95, pp. 431-445, 2016.

[14] C. Buchanan, L. Gardner, "Metal 3D printing in construction: a review of methods, research, applications, opportunities and challenges", Engineering Structures, vol. 180, pp. 332-348, 2019.

[15] T. Skiba, B. Baufeld & O. Van der Biest, "Microstructure and mechanical properties of stainless steel component manufactured by shaped metal deposition", IJIS International, vol. 49, no. 10, pp. 1588-1591, 2009.

[16] T. Niendorf, S. Leuders, A. Riemer, H.A. Richard, T. Tröster, D. Schwarze, "Highly anisotropic steel processed by selective laser melting." Metallurgical and materials transactions B, vol. 44, no. 4, pp. 794-796, 2013.

[17] K. Guan, Z. Wang, M. Gao, X. Li, X. Zeng, "Effects of processing parameters on tensile properties of selective laser melted 304 stainless steel", Materials & Design, vol. 50, pp. 581-586, 2013.

[18] C.Y. Yap, C.K. Chua, Z.L. Dong, Z.H. Liu, D.Q. Zhang, L.E. Loh, S.L. Sing, "Review of selective laser melting: Materials and applications." Applied physics reviews, vol. 2, no. 4, pp. 041101, 2015.

[19] B. Song, X. Zhao, S. Li, C. Han, Q. Wei, S. Wen, J. Liu, Y. Shi, "Differences in microstructure and properties between selective laser melting and traditional manufacturing for fabrication of metal parts: a review", Front. Mech. Eng, vol. 10, no. 2, pp. 111–125, 2015.

[20] C. Buchanan, V.P. Matilainen, A. Salminen, L. Gardner, "Structural performance of additive manufactured metallic material and cross-sections." Journal of Constructional Steel Research, vol. 136, pp. 35-48, 2017.

[21] ASTM, "ASTM F 2792-10 Standard Terminology for Additive Manufacturing Technologies". American Society for Testing and Materials, ASTM International, West Conshohocken, PA, 2010.

[22] S. W. Williams, F. Martina, A. C. Addison, J. Ding, G. Pardal, P. Colegrove, "Wire+Arc Additive Manufacturing", Materials Science and Technology, vol. 32, no. 7, pp. 641-647, 2016.

[23] A. Uziel, "Looking at large-scale, arc-based additive manufacturing", Welding Journal, vol. 4, pp. 42-46, 2016.

[24] C. V. Haden, G. Zeng, F. M. Carter III, C. Ruhl, B. A. Krick, D. G. Harlow, "Wire and Arc Additive Manufactured Steel: Tensile and Wear Properties", Additive Manufacturing, vol. 16, pp. 115-123, 2017.

[25] L. Ji, J. Lu, C. Liu, C. Jing, H. Fan, S. Ma, "Microstructure and mechanical properties of 304 L steel fabricated by arc additive manufacturing", MATEC Web of Conferences, vol. 128, p. 03006, EDP Sciences, 2017.

[26] www.mx3d.com

[27] S.K. Joosten, "Printing a Stainless Steel Bridge: An Exploration of Structural Properties of Stainless Steel Additive Manufactures for Civil Engineering Purposes", Delft University of Technology, 2015 Master thesis.

[28] G.S. van Bolderen, "Exploration of Stability of 3D-Printed Steel Members", Delft University of Technology, 2017 Master Thesis.

[29] I.S. Kim, K.J. Son, Y.S. Yang, P.K.D.V. Yaragada, "Sensitivity analysis for process parameters in GMA welding processes using a factorial design methods", International Journal of Machine Tools and Manufacture, vol. 43, no. 8, pp. 763-769, 2003.

[30] O. Yilmaz, A.A. Ugla, "Microstructure characterization of SS308LSi components manufactured by GTAW-based additive manufacturing: shaped metal deposition using pulsed current arc", The International Journal of Advanced Manufacturing Technology, vol. 89, no. 1-4, pp. 13-25, 2017.

[31] http://rhino3d.com/

[32] W. Ramberg, W.R. Osgood, "Description of stress-strain curves by three parameters" National Advisory Committee For Aeronautics 1943. Technical Note No. 902.

[33] K.J.R. Rasmussen, "Full-range stress-strain curves for stainless steel alloys", Journal of Constructional Steel Research, vol. 59, no.1, pp. 47-61, 2003.

[34] European Committee for Standardization (CEN), EN 1993-1-4:2006+A1:2015 "Eurocode 3 Design of Steel Structures, Part 1–4: General Rules Supplementary Rules for Stainless Steel", 2015.

[35] SEI / ASCE. "08-02. Specification for the Design of Cold-Formed Stainless Steel Structural Members", American Society of Civil Engineering, 2002.

[36] AS/NZS. "4673. Cold-Formed Stainless Steel Structures", Australian/New Zealand Standards, 2001.

[37] Alan Turing Institute to turn the world's first 3D printed steel bridge into a 'living laboratory' for research: https://www.turing.ac.uk/news/alan-turing-institute-turn-worlds-first-3d-printed-steel-bridge-living-laboratory-research [accessed May 2nd, 2019].

[38] H.R. Bae, R.V. Grandhi, R.A. Canfield, "Epistemic uncertainty quantification techniques including evidence theory for large-scale structures", Computers & Structures, vol. 82, n. 13-14, pp. 1101-1112, 2004.

[39] European Committee for Standardization (CEN), EN 10219-2, "Cold formed welded structural hollow sections of non-alloy and fine grains steels-Part 2: tolerances, dimensions and sectional properties", 2006.

[40] European Committee for Standardization (CEN), EN 10162, "Cold rolled steel sections – Technical delivery conditions – Dimensions and cross-sectional tolerances", 2003.

[41] European Committee for Standardization (CEN), EN 10029, "Hot-rolled steel plates 3 mm thick or above – Tolerances on dimensions and shape", 2010.

[42] https://www.artec3d.com

[43] International Standard Organization (ISO), ISO 19902, "Petroleum and natural gas industries – Fixed steel offshore structures", 2007.

[44] V. Laghi, M. Palermo, M. Pragliola, V.A. Girelli, G. Van Der Velden, T. Trombetti, "Towards 3D-printed grid-shells: the main idea and first studies". Proceedings of the IASS Symposium 2018, Boston, USA, 2018.

[45] ISO EN. "6892-1. Metallic materials-Tensile testing-Part 1: Method of test at room temperature". International Organization for Standardization, 2016.

[46] X. Xu, S. Ganguly, J. Ding, S. Guo, S. Williams, F. Martina, "Microstructural evolution and mechanical properties of maraging steel produced by wire + arc additive manufacture process". Materials Characterization, vol. 143, pp. 152-162, 2018.

[47] M. Dinovitzer, X. Chen, J. Laliberte, X. Huang, H. Frei, "Effect of wire and arc additive manufacturing (WAAM) process parameters on bead geometry and microstructure", Additive Manufacturing, vol. 26, pp. 138-146, 2019.

Appendix A

Table A1: Hand measures of thickness of "dog-bone" specimens (Series I and II).

Specimen	Quantities based on caliper measures	
	$t_{av,c}$ [mm]	$A_{av,c}$ [mm]
TI-1-y	2.88	30.76
TI-1-x	2.95	29.39
TII-1-x	4.47	88.44
TII-2-x	4.67	93.33
TII-3-x	4.63	93.13
TII-4-x	4.13	82.67
TII-1-y	4.33	86.67
TII-2-y	4.33	90.13
TII-3-y	4.13	84.32
TII-4-y	4.30	85.57
μ	**4.38**	**88.03**
COV	**0.04**	**0.04**

Table A2: Hand and volume-based measures of thickness of "dog-bone" specimens (Series VI).

Specimen	Quantities based on caliper measures		Quantities based on volume measures			
	$t_{av,c}$ [mm]	$A_{av,c}$ [mm^2]	γ_v [g/cm^3]	$t_{av,v}$ [mm]	$A_{av,v}$ [mm^2]	χ [-]
TVI-1-x	4.47	85.14	7.71	3.56	70.44	1.26
TVI-2-x	4.67	96.00	8.12	3.32	66.33	1.41
TVI-3-x	4.33	84.00	7.79	3.66	73.19	1.18
TVI-4-x	4.33	85.28	7.99	3.55	73.74	1.22
TVI-5-x	4.17	82.00	7.93	3.59	71.88	1.16
TVI-6-x	4.03	75.48	7.84	3.52	71.77	1.14
TVI-7-x	4.30	82.56	7.87	3.79	72.81	1.13
TVI-8-x	4.37	84.00	7.89	3.66	73.18	1.19
TVI-9-x	4.47	118.68	7.99	3.42	94.26	1.31
TVI-10-x	4.43	121.00	7.94	3.66	100.71	1.21
TVI-11-x	4.70	122.40	7.99	3.75	95.74	1.25
TVI-12-x	4.53	129.25	7.99	3.58	98.56	1.27
TVI-13-x	4.93	135.36	7.98	4.50	126.87	1.10
TVI-14-x	4.93	106.22	7.97	4.37	98.67	1.13
TVI-15-x	4.87	110.74	8.02	4.64	104.81	1.05
TVI-16-x	4.60	124.20	7.80	4.13	113.98	1.11
TVI-17-x	4.97	135.24	7.92	4.32	119.21	1.15
TVI-18-x	4.77	141.00	7.99	4.23	126.86	1.13
TVI-19-x	4.93	135.24	7.93	4.26	117.46	1.16
TVI-20-x	4.93	123.97	8.01	4.30	108.82	1.15

TVI-1-y	4.63	98.49	7.37	4.00	80.31	1.16
TVI-2-y	4.13	84.00	7.35	3.99	79.82	1.04
TVI-3-y	4.13	81.60	7.89	3.66	74.59	1.13
TVI-4-y	4.30	91.54	8.04	3.62	72.01	1.19
TVI-5-y	4.10	79.95	7.95	3.62	70.63	1.13
TVI-6-y	4.17	82.32	7.86	3.71	72.74	1.12
TVI-7-y	4.20	84.00	7.78	3.74	74.89	1.12
TVI-8-y	4.33	84.84	7.82	3.72	75.18	1.16
TVI-9-y	4.10	105.20	8.66	3.30	86.90	1.24
TVI-10-y	4.10	107.01	8.72	3.36	87.79	1.22
TVI-11-y	4.10	113.16	7.90	3.69	101.82	1.11
TVI-12-y	4.17	104.14	7.99	3.57	90.79	1.17
TVI-13-y	4.83	107.16	7.95	4.33	98.63	1.12
TVI-14-y	4.67	111.23	7.97	4.29	97.38	1.09
TVI-15-y	4.80	133.00	7.48	4.56	121.40	1.05
TVI-16-y	4.90	130.00	7.72	4.43	115.14	1.11
TVI-17-y	5.03	149.94	7.92	4.40	129.40	1.14
TVI-18-y	5.07	155.55	7.98	4.47	136.43	1.13
TVI-19-y	4.70	121.92	7.98	4.24	107.78	1.11
TVI-20-y	4.63	129.25	7.99	4.23	116.42	1.09
μ	**4.52**	**108.30**	**7.93**	**3.92**	**94.23**	**1.16**
COV	**0.07**	**0.20**	**0.03**	**0.10**	**0.21**	**0.06**

Table A3: measures of cross-sectional area for stub columns (Series III).

	Quantities based on caliper measurements				Quantities based on volume measurements			
Specimen	$D_{av,c}$ [mm]	$s_{av,c}$ [mm]	$A_{av,c}$ [mm²]	$L_{av,c}$ [mm]	γ_v [g/cm³]	$A_{av,v}$ [mm²]	$s_{av,v}$ [mm]	χ [−]
CIII-1	53.59	5.46	825.52	151.63	7.88	609.32	3.90	1.40
CIII-2	54.01	5.45	831.71	149.43	7.87	612.42	3.89	1.40
CIII -3	54.25	5.40	828.78	149.25	7.82	560.65	3.52	1.53
CIII -4	54.22	4.95	765.84	148.19	7.83	598.81	3.78	1.31
CIII -5	53.98	5.31	811.56	152.39	7.82	607.27	3.86	1.38
CIII -6	54.06	5.32	814.26	151.20	7.83	607.15	3.85	1.38
CIII -7	53.83	4.97	762.83	150.97	7.83	609.26	3.88	1.28
CIII -8	54.19	5.46	835.13	151.97	7.82	603.23	3.81	1.43
CIII -9	53.65	4.94	755.61	152.54	7.83	601.61	3.84	1.29
μ	**53.97**	**5.25**	**803.47**	**150.84**	**7.84**	**601.08**	**3.81**	**1.38**
COV	**0.01**	**0.04**	**0.04**	**0.01**	**0.01**	**0.03**	**0.03**	**0.06**

Table A4: 3D-scan measures of BIV-3 tubular element over 40 cross-sections.

Cross-section height [mm]	D_s [mm]	$c_{real,x}$ [mm]	$c_{real,y}$ [mm]	$|c_{real,r}|$ [mm]
20	52.95	-1.03	-0.51	1.15
40	52.95	-0.72	-0.40	0.82
60	52.17	-0.54	-0.46	0.71
80	53.07	-0.63	-0.77	0.99
100	53.37	-1.12	0.11	1.12
120	53.13	-0.59	-0.34	0.68
140	53.92	-0.05	-0.47	0.47
160	53.65	-0.64	-0.52	0.82
180	54.54	0.13	-0.80	0.81
200	53.49	0.19	-0.94	0.95
220	53.96	0.51	0.20	0.55
240	53.50	0.23	0.38	0.44
260	53.14	-0.01	0.24	0.24
280	53.62	0.22	0.28	0.44
300	53.51	-0.53	-0.07	0.54
320	53.77	-0.61	0.18	0.63
340	53.68	-0.76	-0.14	0.77
360	53.68	-0.37	-0.70	0.79
380	53.54	-0.41	-0.52	0.66
400	53.24	-0.17	0.34	0.39
420	54.00	0.01	-0.06	0.06
440	52.98	0.00	-0.13	0.13
460	53.23	-0.71	-0.60	0.93
480	53.62	-0.65	-1.44	1.58
500	53.70	0.19	-0.77	0.80
520	53.21	-0.20	-0.73	0.76
540	53.87	-0.08	-0.25	0.26
560	53.77	-0.85	-0.25	0.89
580	53.59	-1.27	-0.40	1.33
600	53.12	-2.39	-0.82	2.52
620	53.61	-0.89	-1.14	1.45
640	53.32	-1.57	-0.76	1.74
660	53.76	-0.79	-1.16	1.41
680	52.76	-0.79	-1.16	1.41
700	53.64	-1.05	-0.44	1.14
720	53.16	-0.39	-0.16	0.42
740	53.53	-0.24	-0.37	0.44
760	53.40	-0.20	-0.23	0.30
780	53.36	-0.08	0.18	0.20
800	53.60	0.41	0.31	0.51
μ	**53.48**	**-0.46**	**-0.38**	**0.81**
COV	**0.01**	**1.23**	**1.22**	**0.61**

1